University of Bristol - Explore Bristol Research
General rights

Graphical Abstract

Sloshing induced damping across Froude numbers in a harmonically vertically excited system

L. Constantin, J. De Courcy, B. Titurus, T.C.S Rendall, J.E.Cooper
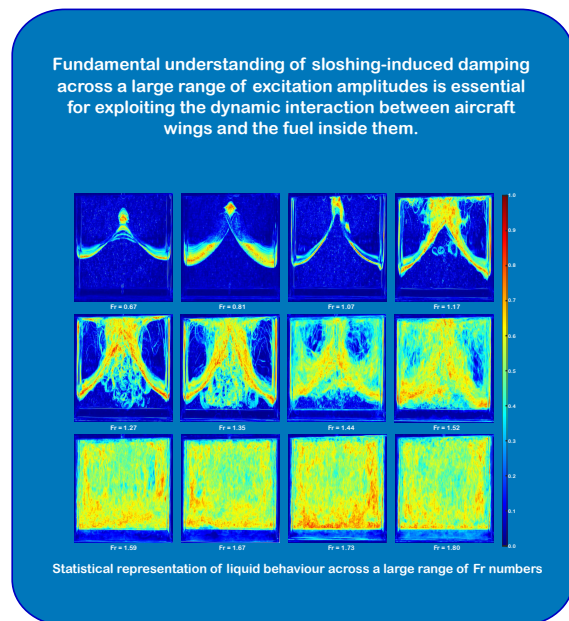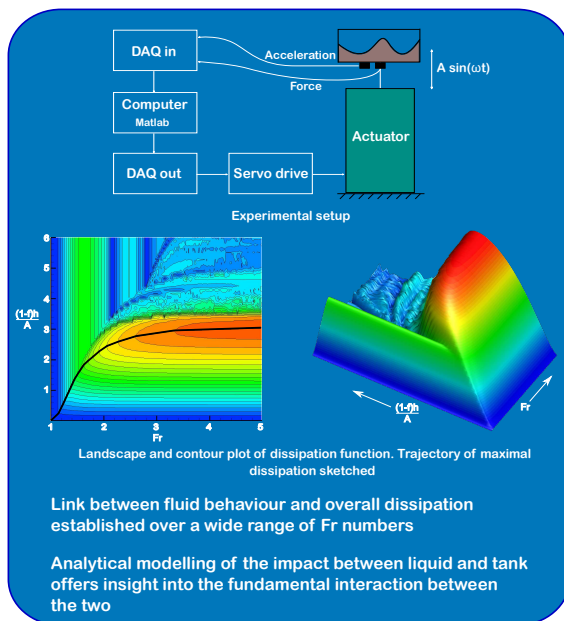
Highlights

Sloshing induced damping across Froude numbers in a harmonically vertically excited system

L. Constantin, J. De Courcy, B. Titurus, T.C.S Rendall, J.E.Cooper

- Sloshing-induced motion and damping across Froude numbers is studied

- Hysteresis cycle analysis reveals liquid motion patterns associated with damping

- Amplitude dependent transition between lateral sloshing to turbulent vertical motion

- Analytical ballistic model helps explain observed effects

Sloshing induced damping across Froude numbers in a harmonically vertically excited system

L. Constantin, J. De Courcy, B. Titurus, T.C.S Rendall, J.E.Cooper

Department of Aerospace Engineering, University of Bristol

Abstract

An investigation was performed to measure sloshing motion and damping during harmonic forced vertical motion of a rectangular tank containing fluid, with a particular focus on the amplitude dependent transition between lateral sloshing and turbulent, vertical slamming. Qualitative and quantitative explanations are provided for the damping saturation point and dissipation effects, together with metrics to distinguish the different sloshing regimes, and a ballistic-harmonic analytical model is presented capable of reproducing the physical trends. Image processing tools were used to analyse experimental high-speed video footage, illustrating potential routes to increased damping in vertically oscillating structures, and correlating well with measured fluid forces and flow regimes.

Keywords: Damping, Sloshing, Loads Alleviation, Parametric excitation

1. Introduction

There is significant current interest aiming to reduce, and eventually eliminate, aircraft emissions and their effect on the environment, with lighter composite structures often playing an important role. These designs can possess lower levels of inherent damping than their metallic counterparts, prompting interest in the damping available from the onboard fuel. Outside aerospace, an understanding of the mechanics of free surface fluid motion, termed here 'fluid sloshing', has received much attention for civil structures to reduce the effect of vibration, primarily through the use of lateral fluid sloshing in an enclosed tank. This activity has now led to increased attention in the use of sloshing in civil aviation, with one specific area of interest being vertical sloshing-induced energy dissipation, or damping, in wing fuel tanks and how to permit lighter, more efficient wing designs. These studies have considered both the gross effect on the added damping to the system, and also more detailed investigations into the mechanics of the fluid-structure interactions and the resulting intricacies in energy dissipation changes.

The influence of fuel sloshing inside wing-mounted tanks has been studied in the past, with an early example of work from Merten and Stephenson [1]. In Merten and Stephenson's [1] work, they studied the effect of sloshing-induced damping in two configurations consisting of beams with tanks attached at the tip. These underwent step-release excitation and consequent bending-only motion; the key findings showed important variations in sloshing-induced damping with filling level and density of liquid, and also that it depends on the transient cycle number,

Nomenclature

ω	Frequency	F_s^t	Total liquid-induced force on the tank
ρ	Density	$F_{s,d}$	Sloshing force
σ	Standard deviation	Fr	Froude number
σ_w	Surface tension	g	Gravitational acceleration
ζ	Damping ratio	H	Height of tank
A	Amplitude	h	Height of liquid column
a	Acceleration	L	Length of tank
C	Cycle domain	m_s	Dry mass
d	Depth of tank	m_w	Fluid mass
E_c	Nondimensional dissipated energy per cycle	N	Number of wall impacts
F	Force	N_c	Number of cycles
f	Filling fraction	T	Kinetic energy
F_e	Excitation force	t	Time variable
f_e	Fraction of energy dissipated in a collision	U	Potential energy
F_L	Force measured by force sensor	v_{rel}	Relative velocity
		x, y, z	Cartesian coordinates
F_s	Sloshing force without inertial component	R1,R2,R3	Damping regions

showing very little dissipation in the first cycle. Widmayer and Reese [2] investigated step-release response of a pitching sloshing system, moving towards the inclusion of the torsional component that is obligatory in flutter analysis; the authors found complex, two-way energy transfers between the liquid and pitching tank, with energy being fed back into the tank at certain times. Both heaving and pitching components were included in Reese's research [3] about the effect of sloshing on a rigid wing mounted on bending and torsional springs, with a pylon-mounted tank. Evidence of sloshing-induced damping was shown, reducing the flutter amplitude with the possibility of increasing the flutter speed. On the same apparatus presented in [3], Sewall [4] then extended the experimental analysis to a wing carrying an internal tank, showing the existence of an optimum fuel-emptying sequence that leads to consistent flutter speed increase for all fuel levels. Sewall's observations were correlated with the fuel modifying the center of mass of the system and the analytical investigations assumed the fuel is a solid mass. Throughout all of these studies,

the influence of the mass moment of inertia of the liquid is seen to be the defining factor in any flutter behaviour modification. Consequently, even today the current industrial practice is to model the fuel as a solid (frozen) mass for numerical analysis, leaving a big gap in understanding the more subtle dynamic interactions between the sloshing liquid and the wing structure under such conditions.

There are multiple non-aviation related instances in literature where sources of energy dissipation in sloshing waves have been studied. Classically, Keulegan [5] showed experimentally that sloshing waves in rectangular basins exhibit exponential decay and attributed the damping sources to viscosity and surface tension effects. Notably in relation to the current work, Jiang et al. [6] and Cavalagli et al. [7] used similar approaches to those described here. Jiang et al. [6] conducted detailed studies of wave-crest breaking and induced damping effects in Faraday waves; the authors found temporal asymmetries and although their study focused on specific symmetry-breaking phenomena, it was found that sloshing surface breaking leads to important additional energy dissipation. Regarding high amplitude/ roof impacting sloshing, work has been done especially in the context of LNG (Liquefied Natural Gas) tanks with the main aim of understanding lateral and ceiling slamming. Rognebakke & Faltinsen [21] studied the high filling level impacting sloshing with emphasis on the influence of air pocket formations when roof slamming occurs. Roof slamming can also occur when the excitation amplitude is low but the filling ratio is high enough, as emphasized in [21], and it can lead to substantial energy dissipation. Rognebakke & Faltinsen [22] showed damping of sloshing motion caused by roof impacts in chamfered tanks and adapted a sloshing analytical model to account for the added damping effect. It was shown that when the liquid impacts the roof, the energy in the jet flow caused by the impact is dissipated. Molin et al. [23] conducted similar experiments on chamfered tanks and their findings suggested that at least part of the induced damping may not be necessarily associated to the roof impacts that were observed. Considering the applications intended in these aforementioned studies (excitation amplitudes and directions typical of LNG tanks), the sloshing amplitudes (and consequently the violence of vertical sloshing motion) are lower than what we consider in the present study.

Cavalagli et al. [7] used similar approaches to those presented here for sloshing force identification and energy non-dimensionalisation, based on hysteresis loop analysis, to quantify energy dissipation trends with varying horizontal excitation frequency. The authors of the work presented here have also conducted previous investigations of a transient single degree of freedom system coupled to a sloshing tank using a novel "T-beam" rig design to achieve vertical large amplitude oscillations after free release [8]. Multiple damping regimes were identified, the first one showing maximum dissipation rates at 0.5 filling fraction and the damping ratio was also studied as a function of peak acceleration and time. A damping saturation point was experimentally demonstrated, and later confirmed using two different numerical models, and after a certain peak acceleration threshold (between 3 and 4g in that case) the sloshing-induced energy dissipation rate was found not to increase substantially anymore. Moreover, Constantin et al. [9] and De Courcy et al. [10] showed both experimentally and numerically how sloshing modes (the first symmetric mode (2,0) [11] in this case) can be used to further dissipate energy in vertical transient experiments at low

amplitudes of motion. The sloshing surface was identified experimentally using a surface tracking algorithm and SPH (smoothed-particle hydrodynamics) simulations confirmed the relationship between the low-amplitude movement of the fluid and additional dissipation effects particularly for such parametric, step-release cases.

A direct application of the sloshing-induced damping effect are represented by the tuned sloshing dampers (TSD). TSDs have been extensively studied with the same idea of exploiting the sloshing-induced damping effects in the field of civil engineering in order to dampen unwanted vibrations in tall buildings, with work being conducted on different types of excitation. For example, Ikeda et al. [12] presented theoretical and experimental results for sloshing-induced dissipation in a horizontally-excited rectangular tank; the authors presented modal equations for sloshing including large amplitude nonlinearity and studied the resonance curves, showing complex behaviour depending on filling level. Bouscasse et al. [13][14] investigated analytically, numerically and experimentally the sloshing of liquids in angular single degree of freedom systems and showed the capability of being exploited in hybrid pendulum mass liquid dampers. Finally, the utility of tuned liquid dampers was proven in an applied case for tall buildings under wind excitation, with Tamura et al. [15] demonstrating the efficiency of TLDs in improving the buildings' dynamic response under daily winds conditions. The literature on TLDs is vast and only a brief selection of the work conducted in the field was presented here.

An important aspect related to liquid sloshing damping is related to tank baffles. For most applications, the liquid action alone inside an empty tank is not sufficient to cause significant damping levels and allow for efficient use as TLDs. The introduction of baffles inside the tank is usually considered to be the main mechanism to increase damping. Various approaches were taken to include the effect of baffles into analytical models of sloshing. Warnitchai & Pinkaew [16] proposed a liquid sloshing model which takes into account low solidity ratio baffles. The solidity ratio is defined as "the ratio of the area of the shadow projected by wire meshes on a plane parallel to the screen to the total area contained within the frame of the screen" [16]. Faltinsen et al. [17] made the argument that oftentimes higher solidity ratios may be desired and, consequently, developed an analytical model to take such baffles into account; satisfactory agreement with experimental results was shown. The literature related to the effects of baffles on sloshing motion control is vast and a comprehensive review is offered in [18]. Multiple studies have been conducted showing various baffle configuration benefits. Simple designs with just one orifice [18] or baffles with multiple slots cut in them [19] have been studied and shown to be effective sloshing dampeners.

Previous research presented in [8] investigated the fluid-induced damping under *transient* conditions through the free response to non-zero initial conditions of a vertically vibrating single degree-of-freedom system. Whilst valuable findings were obtained, the limited degree of control over the test conditions and high sensitivity to the initial conditions at low amplitudes of excitation motivated improvements presented in this study. This work is part of the EU-funded Horizon 2020 SLOWD (SLOshing Wing Dynamics) which aims to gain an understanding of the dynamic interaction between aircraft wing structures and the fuel carried inside. The objective is to avoid unnecessary conservatism in the design loads calculations and enhance gust loads alleviation ability from the sloshing fuel mo-

tion. As a part of the same effort, similar investigations into single degree of freedom systems were completed by Martinez-Carrascal & Gonzalez-Gutierrez [24] and Calderon-Sanchez et al. [25]. They used an SPH-based model and a springs-mass experimental 1DOF system to investigate the influence of various non-dimensional quantities on sloshing-induced damping in vertically vibrating systems with the conclusion that the Froude number and fluid-to-structure mass ratio are the parameters that most influence the sloshing induced dissipation rate. Experiments have been carried out as part of the SLOWD project on multiple degrees of freedom systems as well. Titurus et al. [26] and Gambioli et al. [27] presented a sloshing beam experiment demonstrating additional dissipation effects introduced by the presence of liquid in the system depending on the movement of the fluid and a piece-wise viscous damping response was demonstrated. Development of Reduced Order Models (ROMs) and Equivalent Mechanical Models (EMMs) are also objectives of the SLOWD project, as both valuable insight into the fundamental physics of the problem and useful models that reduce the complexity of full sloshing simulations can be obtained. Constantin et al. [8] have presented an elementary EMM based on a bouncing ball model that satisfactorily modelled the complex vertical interaction between the sloshing fluid and the tank in impact-driven regimes, emphasizing the energy dissipation mechanism. De Courcy et al. [28] then extended the use of this approach to a coupled bouncing ball - aeroelastic wing model and investigated associated dissipative effects in a more realistic model where aerodynamic and structural damping is also involved. Reduced order models have shown as well very good capacity of modelling experimental and numerical results. For example, Mastroddi et al. [29] proposed a ROM based on a generalised sloshing force matrix and validated the obtained results against analytical models. Both EMMs and ROMs are of high relevance in the context of the current work, as they can help to both explain and predict phenomena observed experimentally or in more complex numerical simulations. The modelling approach taken in this work is based on an analytical treatment that describes only the kinematics of the tank and liquid (modelled as a particle) up to the collision point. A similar approach has previously been used in the context of particle impact damping by Friend & Kinra [30] to model the dissipated energy in a beam with a particle-filled container at the tip. Building on this model and on the previously presented EMM of such a sloshing system [8], modelling of the kinematics of the system is found to provide valuable insight into the underlying fluid-structure interaction damping mechanism.

There are three sloshing patterns encountered depending on excitation amplitude and they have been categorised and described in [8]. The sloshing patterns will be reminded here as they will be discussed throughout this work:

- Region R1 – turbulent vertical liquid motion; damping is mainly caused by repeated impacts between the liquid and the tank's bottom and top.

- Region R2 – liquid's movement is dominated by classical sloshing modes, depending on tank geometry, amplitude and frequency of excitation.

- Region R3 – very small amplitude of vibrations, liquid shows close to no movement and no relevant sloshing-induced dissipation effects are noticeable.

This current study is focused on the transition from the classically-studied sloshing motion, denoted in the context of transient experiments as R2, to a more turbulent, vertical and impacting motion (R1). The aim is to deepen the understanding of the damping saturation point and general dissipation effects by studying the transition between R2 and R1 via investigating the qualitative and quantitative differences in fluid behaviour around this point, as well as proposing a particle ballistic model to further explain the nature of the saturation point. The sloshing-induced energy dissipation and its evolution are investigated via a fully controlled vertically harmonically oscillating and partially filled scaled fluid container. Throughout all of this research, the sloshing mode (2,0) was desired to be isolated and studied, since previous transient experiments showed [8] [9] that this particular mode leads to important energy dissipation rates especially if the geometry of the container is suitably matched with its excitation. Of course, asymmetric and higher frequency modes have been previously studied for other applications ([11] offers a comprehensive discussion on this). In this current work, with the help of suitable quantitative indicators, experimental and analytical insights are developed that will support improved models of the sloshing phenomena with intended use in future wing design studies.

This paper is organized as follows: section 2 presents the methodology used in this work and introduces the main concepts used. The experimental setup is presented in section 3 and experiment parameters and strategy are established. Section 4 presents results and analysis of the sets of experiments that were performed. Results based on an analytical model are introduced and discussed in comparison to the experimental data in sections 5 and 6. Finally, conclusions are presented in section 7.

2. Research methodology

This research is presented as a combination of controlled experiments and analytical studies. The tank geometry was carefully chosen so that certain sloshing patterns were evenly spaced and isolated in the frequency range of interest in order to increase the controllability of the sloshing behaviour and to obtain particular steady-state modal responses that are suitable for the analysis presented here. Specifically, the influence of sloshing mode (2,0) was promoted by controlling the length and width of the tank. The ratio of length to width ensures that three-dimensional effects are minimized by separating the out of plane sloshing modes from the mode of interest in the frequency domain. The sloshing mode (m,n) with m nodes in the x direction and n nodes in the y direction (see figure 2 for coordinate system) has the frequency given by the linear sloshing theory [11] as

$$\omega_{mn}^2 = \left(g k_{mn} + \frac{\sigma_w}{\rho_w} k_{mn}{}^3 \right) \tanh(k_{mn}h) \tag{1}$$

where $k_{mn} = \pi \sqrt{(m/L)^2 + (n/d)^2}$, σ_w and ρ_w are the surface tension and density of the working liquid, h is the liquid column height and g is the gravitational acceleration. While equation 1 is based on the linear theory of sloshing which is build on the linear fluid field equations, it is well known that nonlinear effects can lead to resonant frequencies

6

which are different than the linear natural frequencies and are also dependent on the excitation amplitude. Ibrahim [31] offers a comprehensive review on such effects in parametric sloshing. Generally, it was determined that certain types of fluid sloshing can be associated with nonlinear effects such as "*amplitude jump, parametric resonance, chaotic liquid surface motion, and nonlinear sloshing mode interaction due to the occurrence of internal resonance among the liquid sloshing modes*" ([11], page xvi). Moreover, owing to its significance during the transient wing gust response, this study is concerned with parametric sloshing and Faraday waves, the varied parameter being the effective gravity, obtained by exciting the container vertically. This configuration often introduces additional nonlinearities, such as nonplanar, rotational and/ or chaotic motion and disintegration of the free surface. In order to elicit a response on a certain sloshing mode under parametric excitation, the excitation frequency must be close to twice the sloshing frequency of interest.

The excitation amplitude is the most important control parameter studied here while the secondary varied parameter is the liquid filling level. Previous studies [8] showed important dependencies of the sloshing-induced damping on the excitation amplitude, expressed in transient cases as a dependency on the peak acceleration level. In order to generalize the excitation amplitude parameter, and to facilitate later comparisons with other data, the Froude number is used here as a non-dimensional measure of excitation amplitude, representing the square root of the ratio of inertial to gravitational forces and is formulated as a ratio of peak acceleration and gravity such that

$$Fr = \sqrt{\frac{A\omega^2}{g}} \tag{2}$$

where A is the displacement amplitude, ω is the angular frequency and g is the gravitational acceleration.

The Froude number has commonly been associated with fluid surface waves, and was most famously applied by Frederic Reech, and later William Froude [32], for performing correctly scaled experiments to measure wave drag on model ships. Surface waves are often gravitational-inertial in nature, but the Froude number is not intrinsic to fluids and applies equally well to rigid bodies oscillating harmonically in the presence of gravity. Indeed, a particularly interesting non-fluids observation links the transition from walking to running in humans [33] to an appropriately defined Froude number, with similar rules applying to quadrupeds swapping from a trot to a canter. It might also be observed that the Froude number explains why children struggle to keep up with their parents when walking; in fact, both the child's and the parent's transition from a walk to a run occurs at the same Froude number, but this gives a different dimensional speed for each due to their different leg lengths.

Previous research [8] indicated that, above certain amplitudes of excitation, the sloshing-induced damping may be described by the repeated impacts between the liquid and the tank's top and bottom. The damping induced by violent vertical sloshing may thus not be clearly linked to fluid behaviour and may not be explained through reasoning based on fluid dynamics, the impact-based behaviour being largely independent on the nature of the body inside the tank (be it a liquid or a bouncing ball, as discussed in [8]). A ballistic-harmonic model is proposed here to study the kinematics

of impact-driven behaviour, under the assumption that the liquid inside the container is moving as a rigid body.

The analysis presented here is straightforward and makes the assumption that the fluid may be treated as a single lumped mass following a ballistic path within a harmonically oscillating upper and lower wall, as indicated in figure 1. There is no lateral motion and the fluid may not fragment, and no free surface modes are considered. Collisions are treated as inelastic, although it is clearly a significant simplification and one which can only finally be justified by the relative accuracy of the derived model. It has been previously indicated [8] that in such a model a certain impact elasticity is needed to accurately model the energy transfer between the liquid and the tank when such a model is used. However, in order not to complicate the analytical treatment presented here, such elastic collisions are not considered.
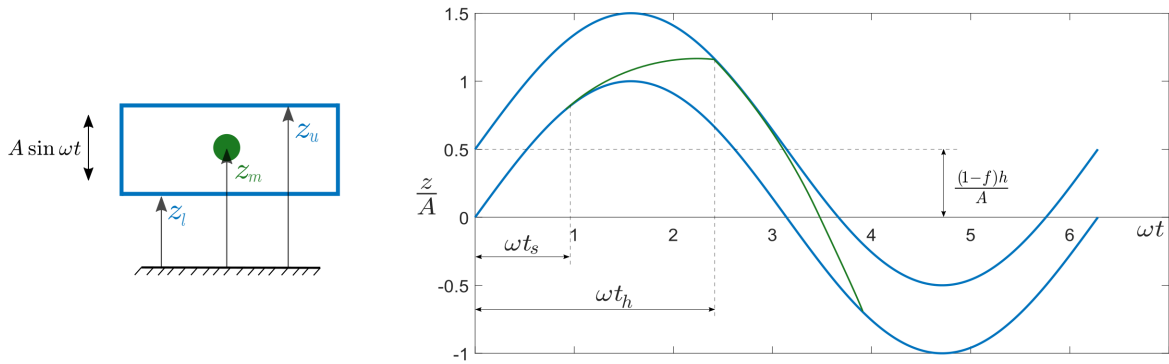

Figure 1: Coordinates and variable definitions for the ballistic-harmonic model

The kinematics of ballistic-harmonic motion are determined by the ratio of inertial to gravitational forces, given by Fr, and the 'headroom' between the free surface and upper wall $(1 - f)h$ (where f is the fraction of the tank filled, and h the tank height), as well as the motion of the upper and lower walls. Written in non-dimensional terms using amplitude A this gives for the single mass of fluid in the z (upwards) direction

$$\frac{z_m}{A} = -\frac{1}{2Fr^2}\omega^2(t - t_s)^2 + \omega(t - t_s)\cos(\omega t_s) + \sin(\omega t_s) \tag{3}$$

where the fluid mass has separated from the lower wall at ωt_s, when the lower wall had speed $\omega A \cos(\omega t_s)$. The walls move according to

$$\frac{z_u}{A} = \sin(\omega t) + \frac{(1 - f)h}{A} \tag{4}$$

$$\frac{z_l}{A} = \sin(\omega t) \tag{5}$$

Specific separation times and collision times are labelled in figure 1, and this nomenclature is also applied in appendix 7 where iterative methods are given for relevant intersections. Increases in Fr cause the ballistic path to become increasingly straight, and increases in $(1 - f)h/A$ cause the upper wall curve to translate upwards, such that these are the two key non-dimensional parameters for this model.

Notably, Friend and Kinra [30] have published the most relevant prior material for the work presented here, which is remarkably not at all related to fluids. In their experimental, numerical and analytical study Friend and Kinra measured the dissipation associated with lead dust (termed 'specific damping capacity' in their work) in a container mounted on the end of a beam. The experimental curves they found are similar to those found later here, and they also went on to calculate the dissipation associated with elastic and inelastic collisions of a lumped mass (modelling the lead dust) in a container. In their work, dimensionless analysis identified a parameter they termed Γ, which can also be identified as the square of the Froude number, alongside a non-dimensional measure of the free space between the lower and upper walls (equivalent to $(1 - f)h/A$ here).

The analytical model presented here will be further detailed in sections 5 and 6 and the experimental force information will be used to test its predictions and to verify the impact-driven behaviour at high Fr numbers.

3. Experimental setup

For each test point presented in this work, the water-filled tank was sinusoidally excited in the vertical direction. Depending on the excitation amplitude and filling level, a steady-state response that shows repeating fluid behaviour and force response in the consecutive cycles can typically be achieved either immediately after the start of the experiment or, in the special circumstances that will be discussed later, after a larger number of observation cycles. Therefore, all of the experiments presented here have been conducted for a sufficiently high number of cycles in order to both eliminate the transient and have a satisfactory number of steady-state periods for a detailed energy dissipation analysis (with an order of magnitude of hundreds of the full tank motion cycles).

Particular to this study, since the excitation force is sinusoidal, the sloshing-induced energy dissipation is determined with the help of the work done by the actuator, during one full steady-state cycle, while displacing the fluid-filled tank. This is equivalent to the area enclosed inside the observed force-displacement hysteresis loops. Typically, within each cycle of oscillation of the tank, there can be a noticeable hysteresis and asymmetry in the sloshing force, in particular when the tank moves up versus when it moves down, measured at the boundary between the tank and the actuator. When calculating the total work done by the sloshing force, the enclosed non-zero area inside each test loop accounts for the dissipative effects that the liquid introduces to the measured system. These effects, up to a small experimental error, are not seen in dry cases as confirmed in the test with the "frozen" mass. The resulting work done per cycle is then nondimensionalized to mass, frequency and amplitude of vibration in order to facilitate comparison with the analytical treatment and transient experiments as well.

3.1. Test rig configuration

A linear actuator is used to impose the controlled vertical sinusoidal motion on the sloshing system. Compared to previous research [8] where highly transient and free vertical vibrations were used, the advantages of using a linear actuator to study sloshing-induced damping are numerous, the most important for this study being:

9

- The ability to focus and isolate a single sloshing mode,

- The ability to study the mode of interest under periodically *steady-state* conditions characterised by the harmonic inputs within certain range of the input frequencies and amplitudes,

- The minimisation of the various parasitic effects such as dry friction and spatial motion irregularity.

The main part of the experimental rig is an electromechanical actuator which is used to introduce the experimental conditions in the form of the prescribed sinusoidal vertical tank excitation. The specific actuator is selected in order to deliver the required test amplitudes and frequencies. The full setup is presented in figure 2. An ETB50 linear electromechanical actuator was used as the actuating element, controlled in velocity by an SV-S servo drive. A PCB 208C03 force sensor was used to measure the force at the boundary between the tank and piston rod of the actuator. A PCB 333M07 single axis accelerometer was used to collect the acceleration information at the same location. An acrylic tank filled with distilled water was fitted at the end of the actuator, on top of the force sensor. The actuator-tank system was then fitted on a custom-built rigid frame, bolted on a Newport RS2000 optical table to ensure vibration isolation from any external source and to limit noise.
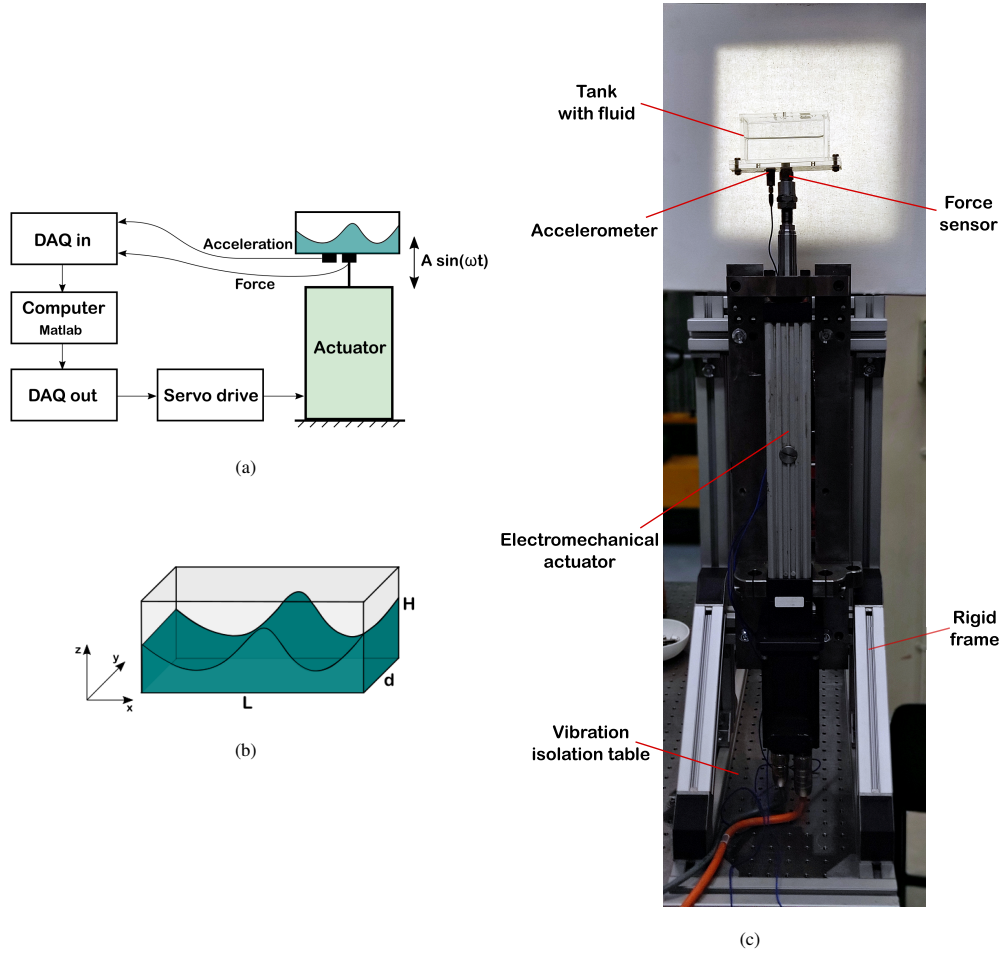
Figure 2: Schematic and photograph of the experimental rig with its main components; (a) Schematic of the experimental rig, (b) Tank dimensions and coordinate system, (c) Photograph of the experimental rig

The force information was collected at the interface between the actuator and the tank. The force system for this configuration is shown in the free body diagram in figure 3. The actuator reaction force F_e is localised between the actuator's piston rod and the sensor. Based on figure 3, this force, which also represents the main observed quantity, is assumed to be in equilibrium with the force F_L which emerges as a reaction between the sensor and the tank. To facilitate focus on the loading effects arising from the fluid-tank interaction in the direction of the applied and controlled motion excitation, a vertical component of the total liquid-induced force on the tank is denoted F_s^t. In principle, this force can represent both the static effect due to gravity and any other superimposed dynamically induced effects which emerge at the interface between the tank and liquid. Then, Newton's second law of motion in the following form can be used to describe the tank motion

$$m_s \ddot{z} = F_L - F_s^t - m_s g \tag{6}$$

where m_s is the structural mass above the force sensor and $\ddot{z}$ is the vertical tank acceleration.
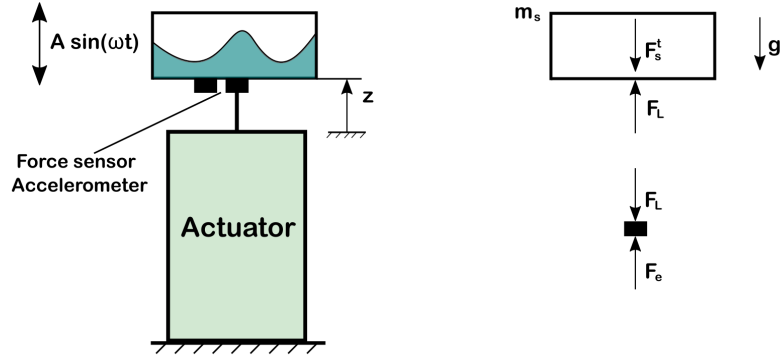

Figure 3: Free body diagram of the sloshing tank system

The force F_s^t is expressed as a combination of the hydrostatic component and the dynamic perturbation component $F_{s,d}$ caused by the combination of the pressure and shear stress interfacial effects at the liquid-tank boundary

$$F_s^t = m_w g + F_{s,d} \tag{7}$$

where m_w is the mass of the liquid inside the tank. From this, the total force observed at the sensor location can be written in the following form

$$F_L = (m_s + m_w)g + m_s\ddot{z} + F_{s,d} \tag{8}$$

The first term on the right hand side represent the combined fluid-filled tank static loading which is not directly measured with the used force sensor. The second term corresponds to the inertial loading of the dry tank when exposed to the non-inertial motion conditions. Finally, the third term represents the investigated dynamic loading from the fluid in contact with the tank which itself can be associated with the imposed non-inertial motion conditions as well as some other phenomena such as the wall shear effects.

For the purpose of the analysis conducted in this work, the fluid inertial force $m_w\ddot{z}$ can be further removed from the dynamic perturbation component

$$F_L = (m_s + m_w)g + (m_s + m_w)\ddot{z} + F_s \tag{9}$$

such that we are left with the sloshing force

$$F_s = F_{s,d} - m_w\ddot{z} \tag{10}$$

12

The sloshing force presented in equation 10 is used when analyzing hysteresis cycles, since the dynamic component $m_w\ddot{z}$ integrates to zero with respect to tank displacement over one tank cycle; in other words, its work done over one cycle is null and thus it does not contribute to the sloshing-induced damping.

3.2. Fluid container design and experiment parameters

Previous experiments conducted by the authors [8] have indicated that, beside sloshing energy dissipation caused by the fluid violently impacting the tank, substantial energy dissipation occurs when the fluid's motion is maintained in one of its sloshing modes. Liquid sloshing modes in rectangular tanks have been documented and studied extensively [11][34], their natural frequencies and linear behaviour being well understood. The tank geometry in this current study is chosen such that the first six sloshing modes (described as (1,0) to (0,3)) up to a frequency of 6.15 Hz are evenly spaced in frequency, as was also explained in section 2.

Based on these considerations, and the discussion in section 2, an acrylic rectangular tank was built with dimensions: $L = 100mm$, $d = 30mm$ and $H = 50mm$ (see figure 2). The mass of the structure (tank, bolts and associated accessories) was $m_s = 185.7g$ and the water mass at 100% filling level was $m_w = 150g$. For a filling level of 50%, this geometry gives a natural frequency of 3.84 Hz for mode (2,0) while keeping other modes' frequencies well separated from it. Consequently, the excitation frequency throughout all of this study was chosen at the value of 8.3 Hz, slightly higher than twice the value of 3.84 Hz obtained using the linear sloshing theory. Preliminary experiments showed that the 8.3 Hz frequency causes the maximum fluid response under all amplitudes analysed. When the excitation frequency was varied, hysteretic effects were observed that depended more strongly on the filling level, with the sloshing liquid responses showing softening or hardening stiffness effects. Consequently, such frequency variations are not considered in this study and are the subject of ongoing work.

The experimental parameters are presented in tables 1 & 2.

Tank geometry [mm]	
Tank height, H	50
Tank length, L	100
Tank depth, d	30

Table 1: Tank geometry

Test conditions	
Filling fraction, f	0.5
Water mass, m_w [g]	75
Excitation frequency, ω [rad/s]	52.15
Excitation amplitude, A [mm]	0.8-12.4
Froude number, Fr	0.47-1.85

Table 2: Test conditions

3.3. Experiment design and test strategy

The objective of these tests is to use harmonic excitation to explore the steady state sloshing behaviour of the tank and the fluid at the resonant frequency of the underlying sloshing mode (2,0) for different amplitudes of excitation using the test set up in figure 2.

The amplitude range was chosen based on multiple factors. First of all, the excitation amplitude dictates the sloshing regime: orderly without surface breaking/ impacting tank ceiling at low amplitudes (R2); transitioning towards impact-driven sloshing pattern with surface breaking at mid-range amplitudes (R2-R1); and strongly turbulent, tank impacting vertical motion at high amplitudes (R1). All of these regimes are captured in this amplitude interval. Second of all, there are considerations related to the equipment used. No amplitudes higher than 12.4 mm could be achieved using this actuator, even though the experimental investigation at the higher Fr numbers would be desirable and might yield useful results. Amplitudes lower than 0.8 mm did not produce a sloshing response and were thus not of interest.

The filling level of 50% was studied here as previous experiments had determined that the sloshing-induced damping is maximized at this filling level in transient experiments [8]. Moreover, by changing the filling level the frequency of the sloshing mode changes as well, complicating the analysis at low Fr numbers. An amplitude range of 0.8 – 12.4 mm was studied here, offering an appropriate Fr number range to enable the investigation of all of the sloshing behaviours of interest. Each sloshing test was conducted for 150 excitation cycles or more in order to reach steady-state behaviour and to have a relevant number of cycles to analyze. Dry tests (no liquid inside the tank) were conducted to measure and characterise a dry energy dissipation.

All of the kinematic information of the system is derived from the accelerometer data. Both an LVDT sensor and a laser velocimeter were tried as well, but both were found to be unsuitable for the application. The LVDT sensor was found to introduce substantial errors in displacement measurements, since placing it at the point of excitation was not feasible. The laser velocimeter was suitable only for the lower range of excitation amplitudes since it was limited in the maximum velocity measurement. For this particular application (purely sinusoidal excitation) the accelerometer data proved to be suffficient. The acceleration signal was band-pass filtered between 5 and 30 Hz. Higher frequency components were associated with the actuator and the test assembly dynamics; lower frequency components were

14

filtered out in order to eliminate any signal bias which, when integrated, leads to error accumulation. The filtered acceleration signal was then numerically integrated once (using the trapezoid rule) to obtain the velocity information and twice for the displacement. All of the collected data was processed using Matlab R2020.

4. Experimental results

A series of experimental results using harmonic excitation to explore the sloshing-induced damping are presented and discussed, based on the methodology described in section 3. A global view of the damping induced by fluid sloshing can be obtained by studying the energy dissipated per cycle, measured as the work done by the actuator over all cycles at the constant amplitude. The value obtained is then divided by the number of cycles in order to obtain an average energy dissipation given as

$$E = \frac{1}{N_c} \int_C F_{s,d} \, dz \tag{11}$$

where C is the set of cycles analysed (the first few transient cycles were eliminated) and N_c is the number of cycles in set C. The same procedure was applied for individual cycles as well in order to obtain information regarding the experimental dispersion of the results. The experimental data was integrated using the trapezoidal rule and the energy is then normalized to liquid mass, frequency and amplitude of oscillation to obtain the normalized energy dissipated per cycle

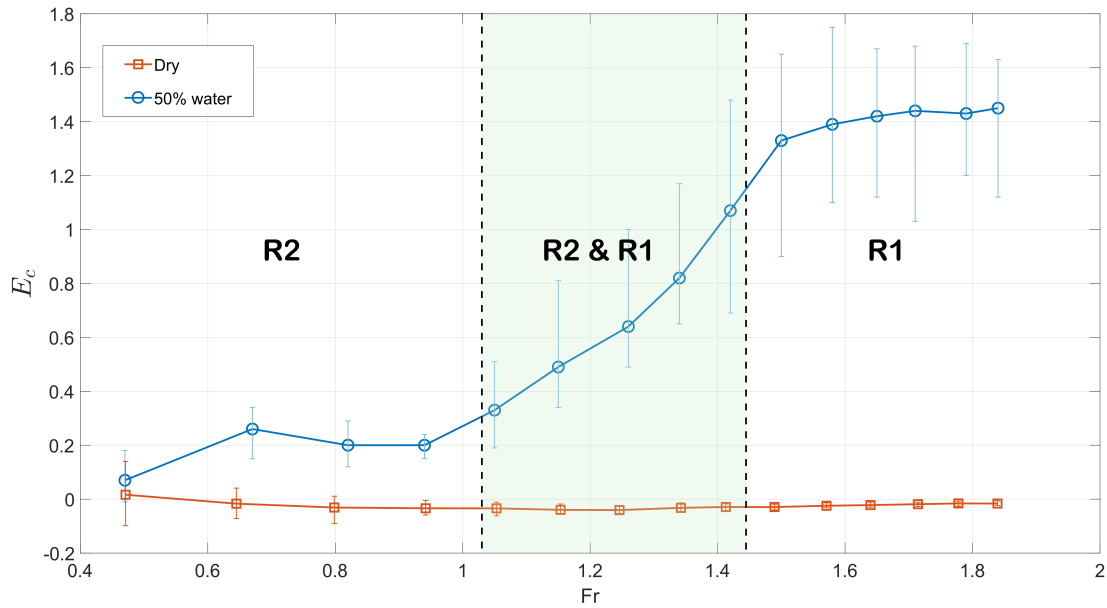$$E_c = \frac{E}{m_w \omega^2 A^2} \tag{12}$$

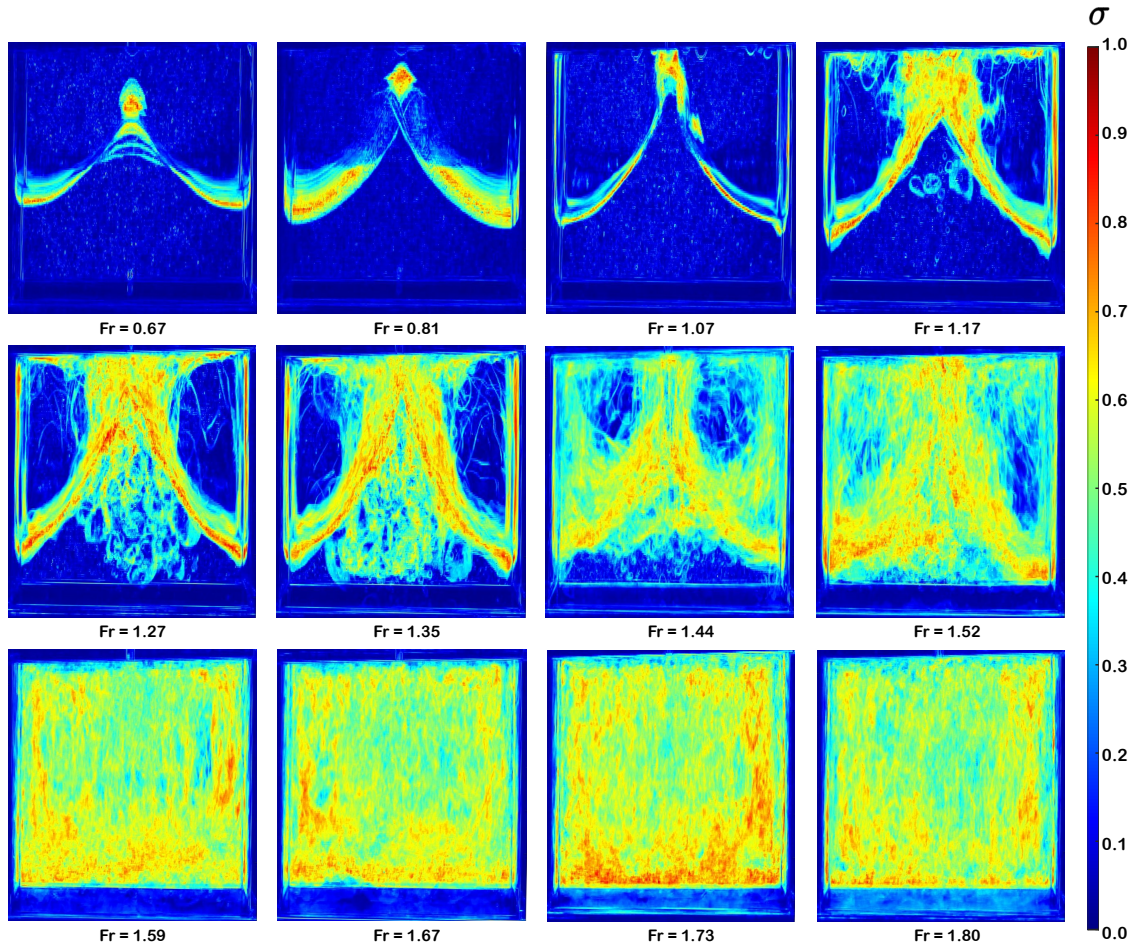Figure 4: Normalized energy dissipated per cycle as function of Froude number

Figure 5: Sequence of figures showing standard deviation of pixel intensity over 25 sloshing cycles for various Froude numbers

A global view of the sloshing-induced damping versus excitation amplitude can be seen in figure 4 showing data for the dry case (no fluid, equivalent mass added to the system) and 50% water filling level. The mean energy dissipation values are presented using markers and connecting lines, calculated using equation 12, and error bars are included as well.

The dry case damping can be seen to have a small value over all Fr numbers and its source resides in the presence of the experimental noise and approximate nature of the collocated input-output (sensor versus actuator rod) configuration. Both, the mean value non-zero bias as well as the error distribution in this quantity decrease with increasing excitation amplitudes associated with increasing Fr number. The dry case decrease in error with increasing Fr number is indicative of varying signal-to-noise ratio and is expected. The wet dissipation values can be judged both in a relative and absolute fashion. In absolute value terms, the energy dispersion is seen to generally increase with amplitude of excitation. At low Fr numbers during R2, the sloshing pattern is dominated by sloshing mode (2,0) and shows little variation from one cycle to the other. The main variation in dissipated energy comes from parametric-induced asym-
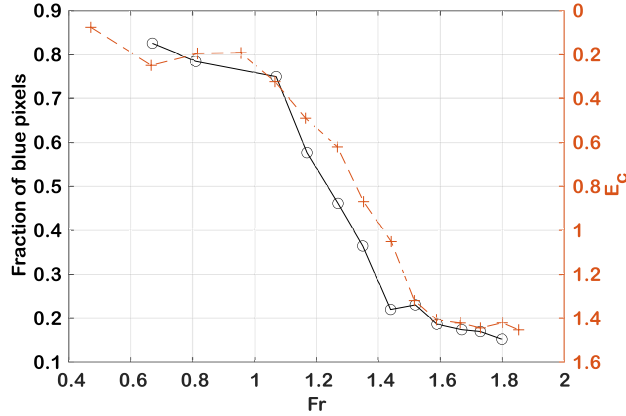
Figure 6: LHS axis: fraction of blue (low standard deviation) pixels for images presented in figure 5. RHS axis: energy dissipated per cycle (from figure 4)

metries, as discussed in detail in section 4.1. Moreover, some level of cycle to cycle variation in dissipated energy is to be expected considering the nonlinear nature of the sloshing regime. Temporal asymmetries and chaotic behaviour was previously noted in literature (see for example [36]). Starting with $Fr \approx 1$ the liquid starts impacting the tank and this is accompanied by an increase in energy dispersion across cycles. Even in terms of errors relative to the mean dissipation energy, looking at the points closest to $Fr = 1$ in figure 4 it can be seen that, as impacts with the tank start happening (in the R2 & R1 combined region) the cycle-to-cycle deviation from mean value increases substantially. This is to be expected, since the impact-influenced sloshing pattern is hard to be consistent from one tank cycle to the next.

To support further visual analysis, Figure 5 presents the statistical fluid behaviour over multiple cycles obtained from slow-motion experimental video captures. For each Froude number, the frame corresponding to the tank's minimum position and the fluid's maximum amplitude was extracted over a number of 25 fluid cycles (50 tank cycles). Each such frame was then converted to grayscale, the standard deviation (σ) of each pixel's intensity was computed over all cycles and then normalized to the maximum value. The results for each Fr number are presented in figure 5, where red values correspond to high standard deviations and blue values to lower ones. Similar techniques based on pixel intensity statistics have been applied for PIV analysis [37].

Figure 4 suggests that the addition of the fluid causes a general increase of energy dissipated with amplitude of excitation. However, three different behaviours of the fluid can be observed when studying the video footage for each case which is presented in more detail in figure 5.

Up to a Fr number of approximately 1, the sloshing pattern is defined by the first symmetric sloshing mode shape (2,0) and this damping behaviour is categorized as R2 according to the notation established in [8]. The normalized dissipated energy is seen to be approximately constant for mode (2,0) with increasing Fr number. The point corresponding to the lowest Fr in figure 4 shows close to no fluid activity, while the Fr = 1.07 point (end of R2) shows maximum activity of mode (2,0) just as impacts with the ceiling of the tank start to occur.

17

The region between Fr = 1.07 and Fr = 1.52 shows an approximately linear increase in the sloshing-induced damping with Fr. This region, while dominated by the mode (2,0) sloshing pattern – R2, also shows impacts with the ceiling of the tank. When the fluid is impacting the ceiling/ floor of the tank, the damping mechanism changes as explained in [8] and is named R1. This happens because the peak acceleration level becomes higher than 1g and the fluid enters the regime which ultimately introduces increasingly strong impact-driven flow turbulence. A combined effect of the two damping mechanisms thus acts at these Fr numbers.

When Fr > 1.52 modal pattern (2,0) (or R2 damping) cannot be observed anymore in the fluid behaviour. The R1 sloshing is then totally dominated by turbulent vertical motion of the fluid and repeated impacts between the fluid and the top/ bottom of the tank. This R1 sloshing-induced damping is found to be relatively constant at higher Fr numbers with only a slight increasing trend being apparent in figure 4. Higher Fr numbers were not attainable in this experiment, so it was not possible to assess the behaviour of the system at higher excitation amplitudes and to establish the damping trend in this region with sufficient confidence. A damping saturation limit is reached at Fr ≈ 1.5 - 1.6, consistent with what was found by the authors in a transient vertical sloshing experiment [8] and also with other transient studies that have found a saturation limit with subsequent decreasing trends [35]. The damping saturation limit is further verified using the analytical model presented in this work. The damping behaviour at higher Fr numbers is subject to ongoing research.

In figure 5, the higher standard deviation (yellow - red) regions correspond to the zones close to the surface, where the light gets refracted as a consequence of passing through the water's surface. Light is not refracted the same way in any two cycles, so the result is an increase in the pixel intensity variation. In contrast, the blue regions are further away from the surface, where the fluid refracts the light the same way over all cycles. What is then obtained is a statistical representation of the water surface over all amplitudes analysed. Figure 5 is thus complementary to figure 4 and reveals a series of interesting phenomena. At low Fr numbers (< 1) the fluid's behaviour is clearly dominated by the first symmetric sloshing modal pattern (2,0). The liquid's amplitude is high and the sloshing regime is non-linear, as evidenced by various phenomena: at Fr = 0.67, a variation in wave amplitude over multiple periods can be observed; at Fr = 0.81, the wave crest can be seen to move horizontally over multiple cycles; these instabilities are to be expected and have previously been noted in the literature. Moreover, the general shape of the waveform and crest are highly altered when compared to the classical linear cosine prediction [11]. The image corresponding to Fr = 1.07 indicates that the wave crest starts to come into contact with the ceiling of the tank; that is the point where the dissipated energy starts to increase substantially (figure 4), as the fluid transitions from a highly ordered and pure R2 regime to a combination of the mode (2,0) pattern and the liquid-tank slamming. Naturally, when the wave starts impacting the top of the tank, surface disintegration and waveform alterations are observed; this happens in the Fr range 1.07 - 1.52. The waveform is seen to increasingly become more inconsistent over multiple cycles, with fluid bubbles arising and turbulence starting to develop. Waveform alterations are accompanied by a constant increase in the dissipated energy, as the fluid - tank impacting interaction becomes more prominent. Starting with Fr = 1.59, mode (2,0) is not discernible anymore and the flow pattern is completely characterised by violent vertical impacting

motion, as also remarked in relation to figure 4. Within the range tested the dissipated energy does not show any substantial increase after this point, indicating damping saturation, as also observed in the transient studies conducted by the authors [8].

The discussion around the statistical representation of the pixel intensity can be further quantified by measuring the fraction of the blue pixels in each image presented in figure 5. The choice for what constitutes a "blue" pixel is subjective but if the same criterion is used for all Fr numbers meaningful conclusions may be drawn. In this case, a blue pixel is considered to have the null red and green components in the RGB representation of the image. The fraction of such pixels that meet this condition is represented in figure 6 as a function of Fr number, alongside the normalized energy dissipated per cycle E_c on the right hand side axis; the E_c axis direction has been reversed in order to better show the relationship with the pixel fraction. There can be seen to be an inversed correlation between the blue pixel fraction and normalized energy dissipated per cycle; as remarked before and as seen now in a quantitative manner, as the surface disintegrates and the flow pattern becomes more turbulent, the sloshing-induced damping increases as well. The proportion of the pixels with the high standard deviation of the pixel intensity increases alongside the dissipated energy. Similar to what is seen in terms of energy dissipation, there is a sharp increase in this standard deviation after Fr =1.07, shown here as a decrease in the fraction of the blue pixels. This fraction is then seen to decrease monotonically up to Fr =1.44 as the sloshing pattern becomes increasingly more turbulent and more interaction occurs between the fluid and the top and bottom of the tank. At higher Fr numbers there is only a slight decrease in the aforementioned fraction, consistent to what is also seen in terms of the energy dissipation per cycle.
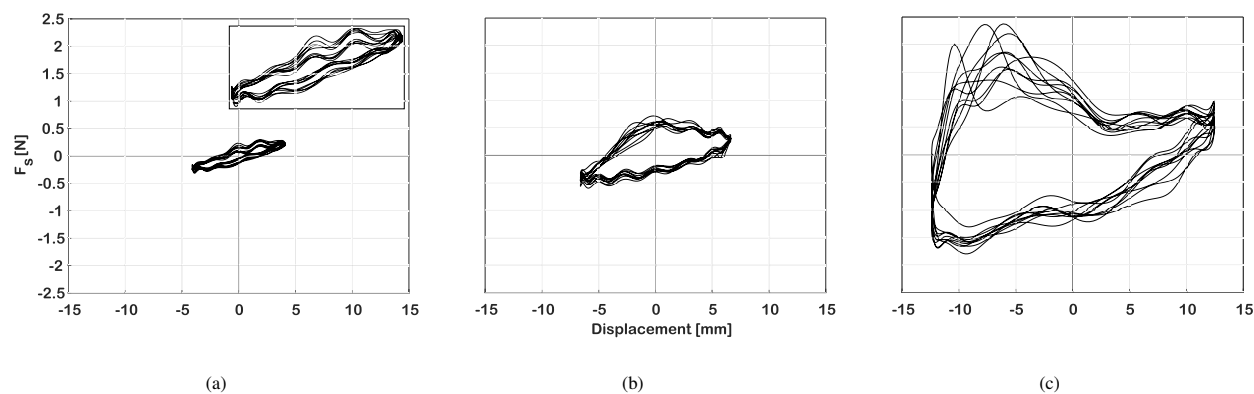

Figure 7: Force - displacement representations over 10 tank cycles for different Fr numbers. A detail of the force loops is included in (a); (a) $Fr = 1.07$, (b) $Fr = 1.35$, (c) $Fr = 1.85$

The sloshing-induced damping can be further investigated by looking at the individual response cycles. While a global representation such as that in figure 4 helps to establish the important damping trends and quantifiers, further insights can be obtained by taking a closer look at the number of consecutive cycles for each Fr number and correlating the observations with the behaviour of the sloshing fluid. Figure 7 shows the sloshing force as a function of the

displacement over 10 complete tank cycles for three different Fr numbers, one per each region identified in figure 4. Considering that the energy dissipated out of the system is measured as the area enclosed in each such cycle (see equation 11), this format clarifies the source of dispersion across multiple consecutive cycles for each Fr number case shown in figure 4. Additionally, it shows clearly the differences in the typical response shape over multiple Fr numbers, consistent with the different fluid behaviours observed in figure 5. Figure 7a shows the hysteresis cycles for region R2 (low Fr numbers). In contrast to the other Fr numbers exemplified here, two distinct response behaviours in the cycle area and shape can be observed; this, as detailed in the next section, is a feature of the fluid's response to the parametric vibration conditions at the low excitation amplitudes. A second observation related to figure 7 is that the maximum force peak moves to the left and the overall shape becomes increasingly assymetric relative to the origin of the coordinate system with an increase in Fr number, suggesting the occurrence of the distinct dynamic phenomena in the different parts of these response cycles.

Multiple rich phenomena can thus be observed by studying the hysteresis cycles. In what follows, representative cycles for each region delineated in figures 4 and 7 (R2, R2&R1 and R1) are analysed separately.

4.1. Region R2 - low level excitation

Figure 8 shows two representative tank cycles for a Fr number of 1.07, where the steady-state response dominated by mode (2,0) reaches its maximum level without coming into contact with the roof of the tank. Analysis of a single tank cycle is not sufficient in this case because, due to the nature of parametric vibration, the fluid sloshes at the half of the frequency of excitation. One fluid cycle will thus occur over two excitation (tank) cycles and so there exists the possibility of asymmetries in the damping characteristics between the two consecutive cycles as can be seen figure 7a.

The sloshing force response is represented here in multiple forms: hysteresis force-displacement (8a) and force-velocity (8b) loops, where the time parameter is eliminated, as well as the force and velocity time series (8c and 8d), respectively. Figures 8a and 8b show the discrepancy in the sloshing-induced dissipation over two tank cycles. The points of minimum (A) and maximum (B) force over both cycles have been marked in the figures, as these are the points of interest to be correlated with the fluid behaviour, especially at higher amplitudes. Here, the minimum/ maximum points are referred to considering the sign of the sloshing force and not in the sense of absolute values. As in figure 3, the sloshing force is considered positive when it acts downwards. The displacement and velocity sign conventions follow the positive upwards z direction. The force is seen to be maximized in the proximity of the point where the tank reaches maximum velocity during the first forcing cycle where the fluid pushes against the bottom of the tank, as can be qualitatively seen in figure 9, where green arrows were introduced to show the general direction of motion of the sloshing surface at that specific time instance; this is a prevalent feature that will be observed across all Fr numbers and fluid sloshing patterns. The force is minimized when the wave's amplitude reaches its maximum/ minimum, as can be also seen in figure 9 (points A_1 and A_2). The second tank cycle (with dashed line in figure 8) has a hysteresis loop half as large as the first one, with normalized dissipated energies of $E_{c1} = 0.45$ and $E_{c2} = 0.24$ respectively. Their average is seen to correspond to the $Fr = 1.07$ point in figure 4, however, this discrepancy in the

enclosed area of the displacement-force loops between the two consecutive tank cycles is investigated in more detail next.
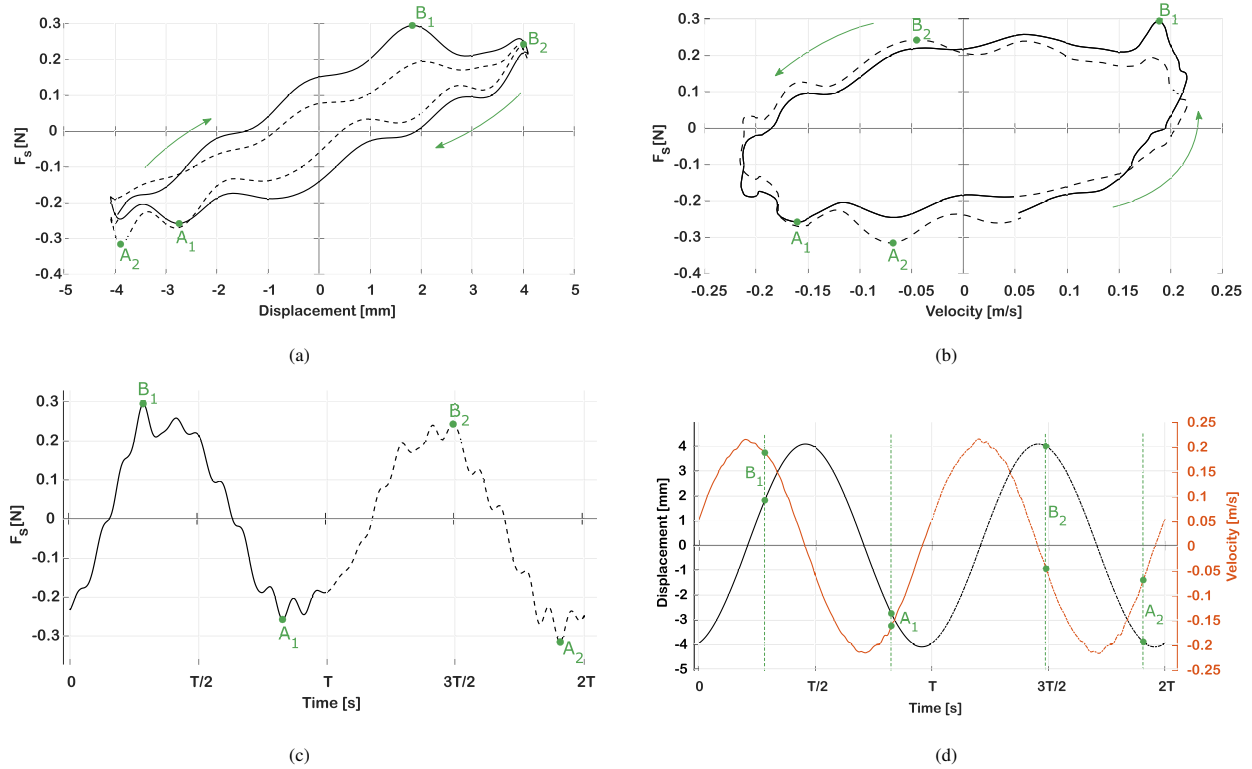

Figure 8: Force, displacement and velocity for a representative sequence of the two consecutive tank cycles in R2 region, $Fr = 1.07$; (a) Sloshing force vs. tank displacement $F_s(z)$, (b) Sloshing force vs. tank velocity $F_s(v)$, (c) Sloshing force vs. time $F_s(t)$, (d) Tank displacement and velocity vs. time $z(t)$, $v(t)$
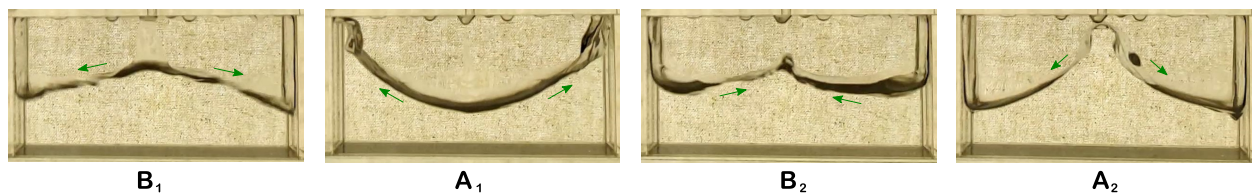

Figure 9: Sloshing snapshots for the points presented in figure 8

The energy dissipation discrepancy in this case is due to waveform alteration at high sloshing amplitudes. For small amplitudes of vibration, the (2,0) sloshing mode wave form in a rectangular tank has a well-known cosine shape [11]. However, in this case of the high amplitude motion, the sloshing surface is seen to be altered, with the crest deformation and the pronounced boundary region presence up to the tank's ceiling, as can be seen in figure 9. Such features have previously been noted in the literature (e.g [6], [38]). Moreover, one of the most important sources of energy dissipation in sloshing waves comes from the viscous dissipation at the boundary of the fluid and the

surrounding tank [40]. It is thus worth taking a more detailed look at the behaviour of the water surface across one fluid cycle. The authors have previously presented a sloshing surface tracking algorithm that was used to gain insight into the surface mid-point displacement in relation to the containing tank, under transient parametric excitation. For a full description of this algorithm, see [9]. The same algorithm was applied here, and in this case the right-hand side surface boundary point is analysed. An example of the identified surface in one frame is presented in figure 10a. The water surface was tracked across all video frames within the tank cycles presented in figure 8 and the vertical (z) displacement of the right-hand side (RHS) boundary point relative to the tank is shown in figure 10b. The raw displacement results were obtained in terms of the number of pixels and the values in millimeters were estimated based on the known height of the tank.
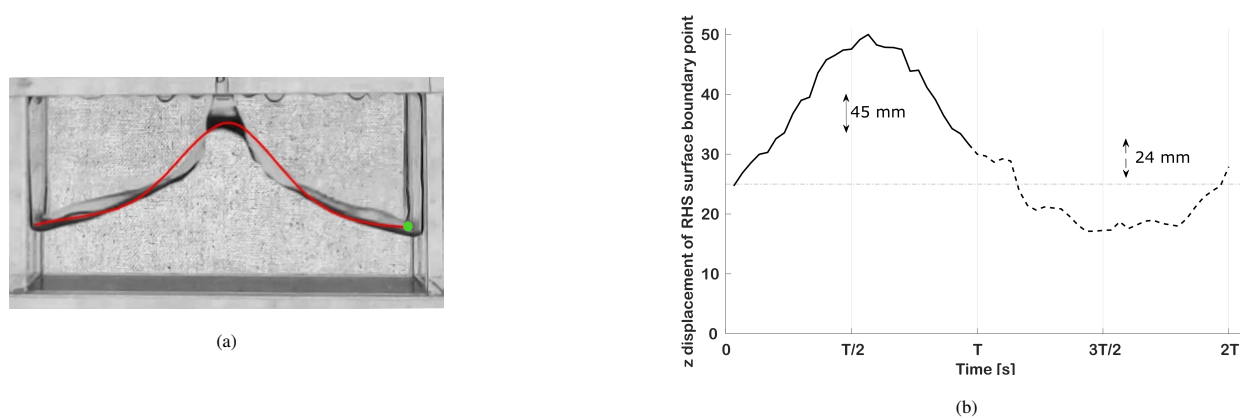

(a)

(b)

Figure 10: Tracking of the RHS surface boundary point across the two tank cycles; (a) Example of the identified sloshing surface. Green point is tracked. (b) Vertical displacement of the RHS surface boundary point relative to the tank

A clear asymmetry in the boundary point displacement can be seen. Considering that a major source of energy dissipation (perhaps the most important in this case) is represented by the shearing action between the fluid and the tank at its boundary, this asymmetry is likely linked to the energy dissipation disparity. Indeed, looking at the total travel distance of the boundary point relative to the tank in each of the two tank cycles, we see that in the first tank cycle it travels for approximately 45*mm* as the sloshing surface reaches the top of the tank and then returns; on the other hand, as the fluid retracts and completes the full parametric cycle, it travels for a total of only approximately 24*mm* relative to the tank. The ratio between the two travel distances of the boundary point is thus $\approx 1 : 2$, close to the ratio of the normalized dissipated energies, suggesting that there is more shearing between the sloshing liquid and the tank in the first tank cycle leading to more energy dissipation.

Hysteresis force-displacement and force-velocity plots, like those shown in figures 8a and 8b, provide complementary insight into the physical processes observed during the fluid sloshing. In this case, both figures evidence visco-elastic response of the fluid in the form of a pair of the two distinct and periodically repeating tank cycles.

One cycle, with the larger enclosed displacement-force area, corresponds to a more dissipative regime, while the subsequent cycle, with the smaller enclosed displacement-force area, corresponds to a regime with more pronounced spring-like behaviour. This can be corroborated with the corresponding velocity-force loops, figure 8b, which can be closely approximated by two similar rotated ellipses where an increasing time parameter implies counterclockwise motion across the loops. This behaviour is characteristic of systems with the constituent linear elastic and viscous force sources. Further correlation of these findings is shown in figure 8d where the peak force responses lag behind the peak motion inputs due to the described visco-elastic effects produced by the system in the R2 sloshing regime.

4.2. Transition region R2-R1 - medium level excitation

As the exctitation amplitude increases, the fluid starts impacting the top of the tank and the surface is consequently broken. This impacting interaction leads to a substantial increase in energy dissipation. The region between $Fr \approx 1$ and $Fr \approx 1.5$ sees a monotonic increase in energy dissipation per cycle as the sloshing pattern becomes increasingly dominated by the vertical motion of the fluid and slamming into the tank. This is a transition region, as both R2 and R1 behaviours are seen to be overlapped.

Figure 11 shows the force response for the $Fr = 1.35$ case in multiple forms, as also discussed in relation to lower Fr numbers and figure 12 shows the sloshing snapshots at the times of interest. It is noteworthy that, even though the influence of mode (2,0) can still be seen in the sloshing pattern, analysis of two tank cycles is no longer needed as there is no discernible variability attributable to this phenomenon in the measured response from one cycle to the next. The size of the hysteretic cycle itself increases substantially (see figure 7) and the impacting interaction dominates over any variability that may be introduced by the parametric vibration conditions. Nevertheless, the snapshots for two tank cycles are shown for the extreme force responses in figure 12 for completeness.

The force-displacement and force-velocity cycles change shape as compared to lower Fr numbers, as the maximum force point (B) moves to lower displacements. Maximum response in force is obtained when the tank reaches maximum velocity during ascension and the liquid pushes against the bottom of the tank, as can be seen in figures 11b,11d and visually in figure 12. Green arrows were introduced in figure 12 to show the instantaneous direction of motion of the sloshing surface. The minimum sloshing force response is obtained at the minimum stroke of the tank and its absolute value is roughly equal to the maximum force. Furthermore, it was remarked earlier that two tank cycles are not necessary here because the hysteresis loops do not present much dissimilarity from one cycle to the next; however, in figure 12 it can be seen that the fluid's behaviour is quite different among consecutive cycles. The explanation resides in the fact that, even though the influence of mode (2,0) can still be seen in this Fr range, the impact-driven behaviour dominates the force response here, leading to indiscernible asymmetries between consecutive tank cycles. This can also be seen in the three regions comparison from figure 7, where the cycles corresponding to Fr = 1.35 are markedly bigger than those corresponding to Fr = 1.07. Even though visually the fluid behaviour is dissimilar in the two consecutive cycles, due to the fluid-tank impacts this parametric vibration-driven asymmetry is
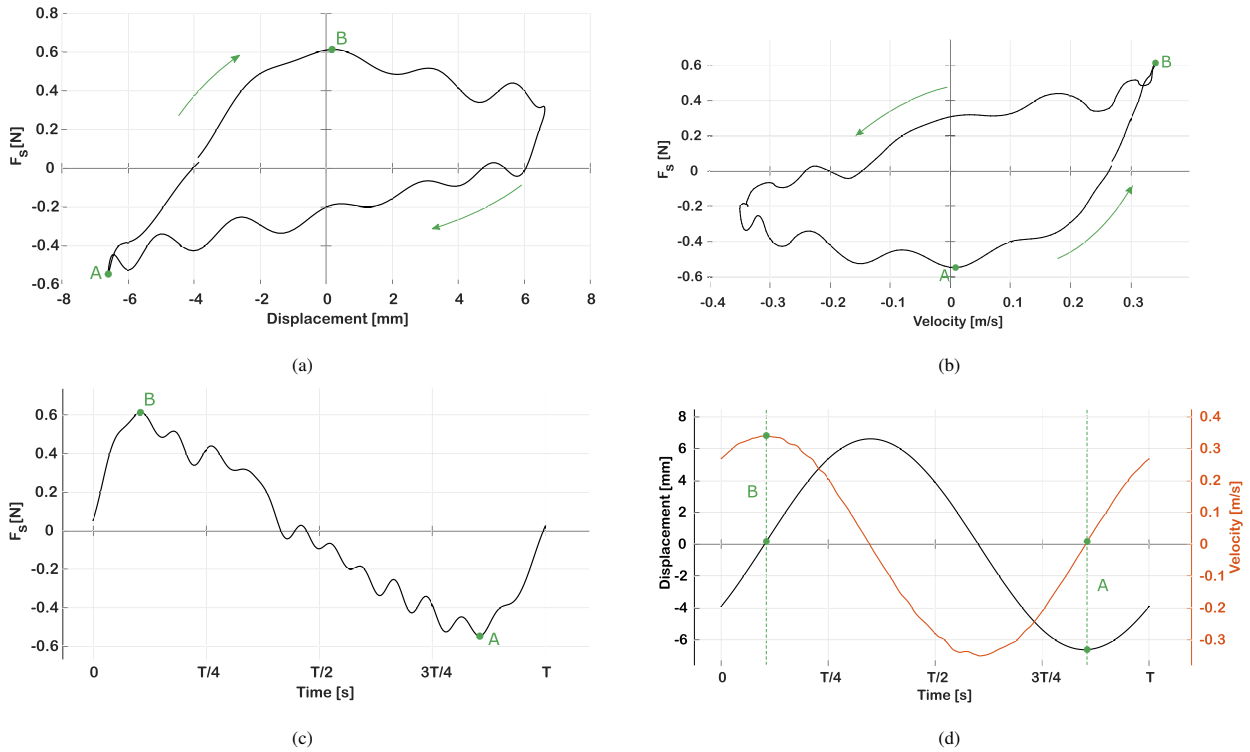
not visible in the sloshing force response.

Figure 11: Force, displacement and velocity for a combined R2&R1 representative tank cycle, $Fr = 1.35$; (a) Sloshing force vs. tank displacement $F_s(z)$, (b) Sloshing force vs. tank velocity $F_s(v)$, (c) Sloshing force vs. time $F_s(t)$, (d) Tank displacement and velocity vs. time $z(t)$, $v(t)$
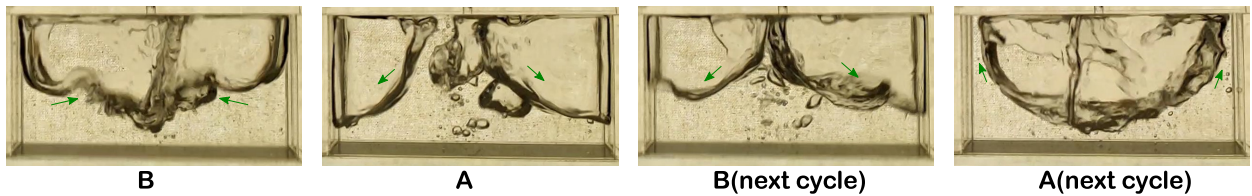

Figure 12: Sloshing snapshots for the points presented in figure 11

Whilst gravity in the previous case contributed toward the parametric vibration conditions where the individual constituent cycles featured notably symmetric behaviour, gravity in this case introduces significant asymmetry within each measured tank cycle as can be seen from the force-displacement, figure 11a, and force-velocity, figure 11b, plots. With reference to figure 11b, an increasing time parameter still implies counterclockwise motion across the loop suggesting thus the dominant influence of the visco-elastic force sources, in particular on the trajectory from point B to point A. However, the transition from point A to point B can be associated with the inertial effects and liquid-tank momentum exchange. This finding is supported by the emergence of the small clockwise sub-loop around point B in the same figure, and by relatively unchanged waveform when transiting from A to B(next cycle) and from A(next

24

cycle) to B, see figure 12. The motion-induced transition is faster than the rate at which the wave changes its shape and the wave maintains its main features under given inertial forcing. This effect further expands under the R1 sloshing conditions.

4.3. Region R1 - high level excitation

As the excitation amplitude increases furthermore and we get past the damping saturation point, no discernible trace of mode (2,0) is left and the sloshing pattern is completely dominated by the vertical turbulent and impacting motion of the fluid. Figure 13 shows the same force information as for the other cases analysed before, for a Fr number of 1.85 and one representative tank cycle. Figure 14 shows two snapshots for points A and B to illustrate the qualitative behaviour of the fluid within the cycle, with the green arrows showing the general direction of the liquid at that time instance.
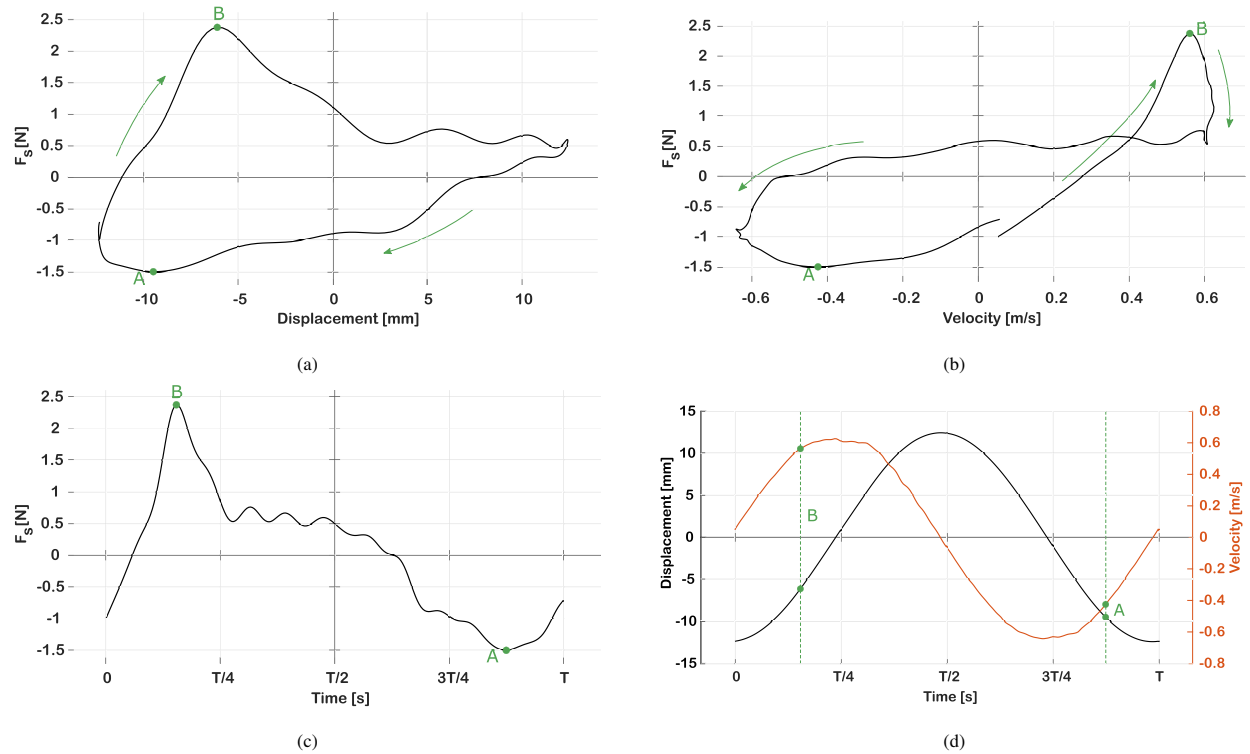

Figure 13: Force, displacement and velocity for a R1 representative tank cycle, $Fr = 1.85$; (a) Sloshing force vs. tank displacement $F_s(z)$, (b) Sloshing force vs. tank velocity $F_s(v)$, (c) Sloshing force vs. time $F_s(t)$, (d) Tank displacement and velocity vs. time $z(t)$, $v(t)$
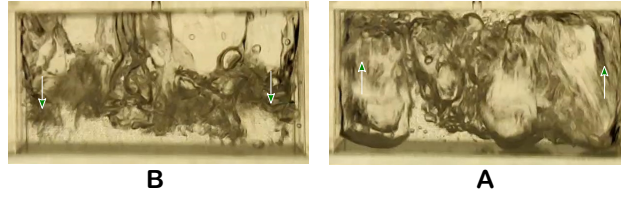
Figure 14: Sloshing snapshots for the points presented in figure 13

The most striking feature when analysing the hysteresis cycles is the prominence of the maximum force peak (B), as seen in figures 13. As also noted in relation to the transition region R2-R1, the sloshing force is maximized when the fluid impacts the bottom of the tank immediately after the tank reaches its minimum position. Something particular is evident here: there is a notable difference in the absolute values of the minimum and maximum sloshing force ($F_B = 2.4N$ and $F_A = -1.5N$). This force asymmetry is more substantial compared to the previous cases and suggests that different interactions between the liquid and the tank may contribute more to the total energy dissipation. A statistical representation of the fluid at points A and B, based on the pixel intensity standard deviation and similar to what was shown in figure 5, is presented in figure 15, where an intermediate frame between the two points is included for reference. Similarly to what was discussed earlier in the results section, the low standard deviation (blue) pixels indicate the consistent presence of a body of liquid over multiple cycles. It can be seen that, at point B, the fluid is on average found near the bottom of the tank, while at point A it is near the top of the tank. This behaviour supports the observation that the sloshing force peaks when the fluid impacts the bottom and top of the tank, as expected. Moreover, the standard deviation is seen to be lower at point B, near the bottom, when compared to point A near the top, which means that generally more liquid impacts the bottom of the tank at point B than it impacts the top at point A. This is due to gravity aiding the fluid's impacting motion with tank's bottom and correlates well with the asymmetry in sloshing force peak values. In contrast with snapshots A and B, the intermediate snapshot from figure 15 shows the fluid being distributed relatively evenly across the vertical coordinate of the tank.
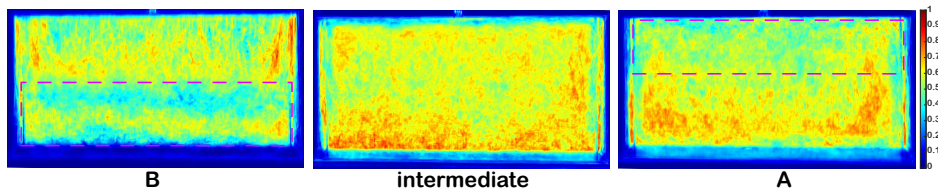

Figure 15: Standard deviation of pixel intensity over 50 tank cycles

Overall, the degree of response asymmetry increases compared to the mixed R1-R2 regime. Referring to figures 13a and 13d, it can be seen that the majority of the sloshing work is done in the left half-plane in figure 13a which corresponds to the interval between 3T/4 and T/4, i.e. the bottom half of the tank's motion cycle. Figure 13b now features fully developed self-crossing hysteresis loop. This feature is associated with the phasing change between the peak velocity and peak force. While in the R2 region the maximum force was seen to be achieved after the velocity

26

peak and in the R2-R1 transition case the two were coincident, at higher Fr numbers the maximum sloshing force is obtained before the maximum velocity is reached, as can be seen in figures 13b and 13d. This behaviour is a consequence of the fact that at high Fr numbers the fluid impacts with the bottom of the tank occur soon after the tank's minimum displacement is reached and the liquid comes down aided by gravity and violently impinges on the tank's floor. As discussed in the previous section, by now the well-developed self-crossing loop with the ensuing clockwise motion with the increasing time parameter across the velocity-force loop, figure 13b, is indicative of the dominant effect of the momentum exchange between the bulk of the liquid whilst being combined with intense turbulent mixing arising from the broken surface of the previously stable and dominant (2,0) waveform.

4.4. Comparison with transient experiments

Finally, a comparison between the forced experiments presented here and a series of transient experiments is made. The authors have previously described a transient "T-beam" experiment [8], as discussed in the introductory part of this work. There, different filling levels were investigated and the equivalent damping ratio has been experimentally measured for each filling level and different Fr numbers. For comparison purposes, the energy dissipated per cycle can be obtained from the damping ratios presented in [8]. This is done, as explained in Appendix 7, under the hypothesis that ζ is constant throughout the transient motion; only the first part of the transient (as also presented in [8]) is considered here for comparison with the sinusoidal excitation data. An equivalence formula can thus be obtained as follows (for full derivation see Appendix 7)

$$E_c = \frac{1}{2}\frac{k}{m_w\omega^2}(1+\zeta^2)(e^{-4\pi\zeta}-1) \tag{13}$$

Similar to what was shown in the previous sections, forced excitation tests were carried out for the 30% and 70% cases for comparison purposes. Using the conversion relationship (equation 13) and representing all of the data for the three filling levels analysed, the comparison for the normalized energy dissipation per cycle is presented in figure 16.

The comparison between the two sets of data is limited in Fr number, as higher amplitudes were not achievable using the experimental setup presented in this work. However, the asymptotic behaviour of the two systems, as the Fr number increases, corresponds well and the overall correlation between the two sets of data is very good. As expected, the most notable differences appear in the low Fr number range where the water sloshing mode is defined by the geometry of the tank. The most extreme instance is seen at the 30% filling level where, due to the chosen geometry of the present tank, the sloshing mode (0,1) also gets excited at $Fr \approx 1$ and, as a consequence, E_c is seen to increase substantially in that region. This condition is a mere result of a particular combination of the tank geometry, filling level and Fr number - a combination which was not the same in the transient case. Moreover, the 30% filling level and $Fr \approx 1$ case was seen to be particularly affected by the strong modal competition. When the subharmonic response of the liquid is studied at the high amplitudes, such as in this case, the stability boundaries of each characteristic sloshing mode constitute the so called Ince-Mathieu frequency-amplitude chart [39]. The regions
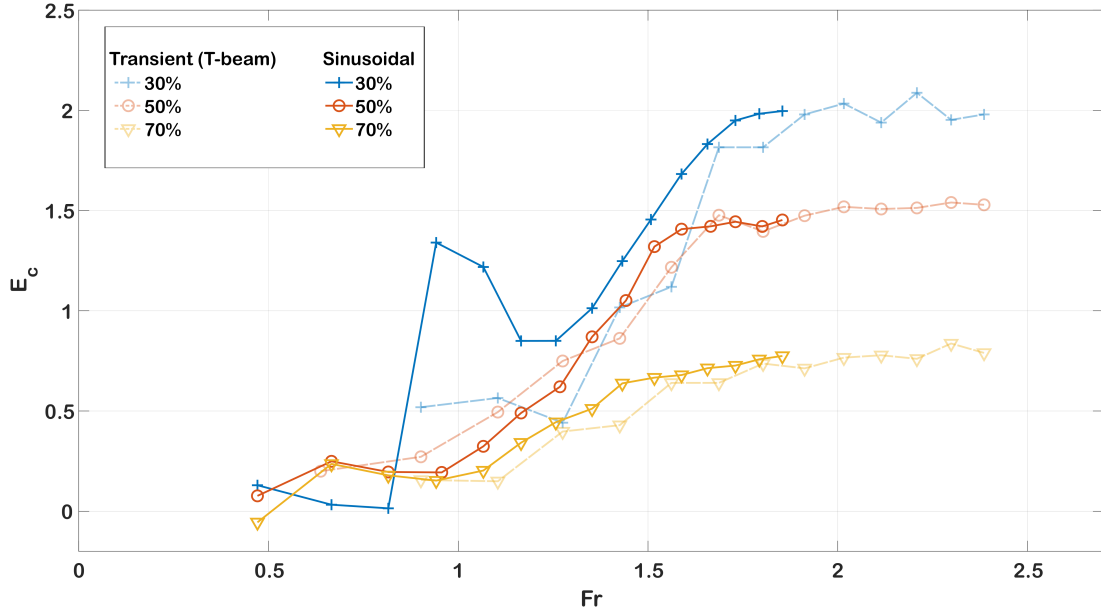
27

Figure 16: Normalized energy dissipated per cycle vs Fr, transient versus sinusoidal excitation

corresponding to different modes typically overlap above certain excitation amplitudes. In the experiments discussed here, the associated amplitude-sensitive behaviour was observed in the form of the multiple dominant modes being transited through when arriving at the particular steady-state response regime.

Figure 17 shows selected characteristic snapshots around four different time instances indicated via the tank cycle number. The liquid's response is initially typical of mode (2,0) but an instability in this mode soon develops, leading to the birth of a longitudinal wave (cycle 91). The sloshing pattern then evolves further into an asymmetric mode (cycle 100) with the water reaching the ceiling of the tank, a highly atypical behaviour for this Fr number. By reaching cycle 128, the fluid transitioned to the mode (0,1)-dominated sloshing behaviour, oscillating at very high amplitudes in the tank's width direction (y) and combined with the ceiling impacts. This relatively stable response was observed for the rest of the test, constituted by approximately 400 additional tank cycles. Similarly to all other Fr numbers and filling levels analysed, the sloshing-induced energy dissipation was measured only after the response of the fluid stabilised at the particular sloshing mode, in this case characterised by the (0,1) modal pattern. It is important to reiterate that this case was unusual in terms of the time required to reach a stable sloshing pattern and the competition observed between the multiple modes. This situation was not observed for other parameter combinations.

Moreover, as mentioned before, the transient experiments presented in [8] have shown that the damping ratio is maximized at 50% filling level. Here we see that, even though the damping ratio (decay rate) is maximized at one filling level, the dissipated energy normalized to water mass, equation 12, is not necessarily maximized at the same filling level. This is the consequence of normalization to water mass, which decreases with the filling level.
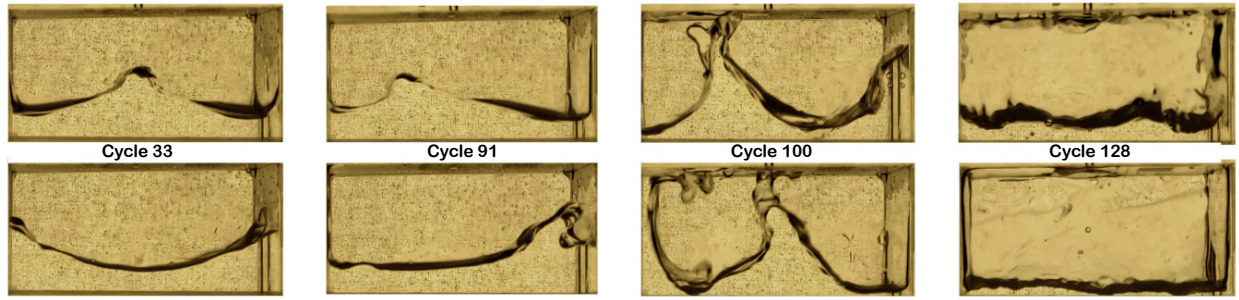
Figure 17: Snapshots with sloshing behaviour at multiple time instances for filling level 30% and $Fr = 0.94$

Of course, from the point of view of the transient applications such as the aircraft fuel sloshing due to atmospheric gusts, the sloshing-induced damping ratio is desired to be maximized. Drawing on the analogy with a simple ball vibrating in a box (see section 5 on the ballistic-harmonic model) the maximum kinetic energy that the tank could impart to the liquid inside the box if there were no ceiling would be $0.5 m_w \omega^2 A^2$, such that the normalization used here (equation 12) could be interpreted as a measure of the dissipated energy relative to the maximum that the could theoretically be transferred from the tank to the liquid as it projects it on the parabolic trajectory, if the liquid were behaving as a rigid mass.

Another important aspect evident from figure 16 is that the damping saturation limit is inversely proportional with the filling level. In other words, there is a Fr number limit above which the non-dimensional energy dissipated by sloshing does not increase substantially anymore, and this limit decreases with increasing filling level. The results discussed here indicate that this limit is reached when the fluid starts to fully impact the ceiling of the tank without any trace of an R2-characteristic sloshing mode left. With increasing filling level the fluid surface is closer to the tank's ceiling and impacts it at lower amplitudes. Consequently, the saturation limit moves towards lower Fr numbers. This finding will be further verified using the analytical impact model introduced in section 2.

Finally, the energy dissipation data presented here in the normalized form shows that the available liquid kinetic energy to be dissipated decreases with filling level, as expected. In the limit at 100 % filling level, the liquid would have no room to move inside the tank and no energy dissipation would be possible. This result is also confirmed by the results presented in [8], where the dissipation rate was shown to vary parabolically with filling level with a maximum at 50% for the case of purely vertical excitation at high Fr numbers. This fact has the further potential to inform future equivalent mechanical models, where a coefficient of restitution or equivalent liquid mass may be used.

5. Ballistic-harmonic collisions

It is clear that violent sloshing behaviour shows certain dissipation trends that are not easily explained through reasoning based on fluid dynamics, or which at least do not clearly link to fluid behaviour. Analysis of the experimental force information across tank cycles showed that at high Fr numbers the liquid-tank impacting behaviour is the main

driver of energy dissipation. It is therefore reasonable to consider that the kinematics of the motion may be at least equally important to the fluid dynamics and may usefully be considered in isolation.
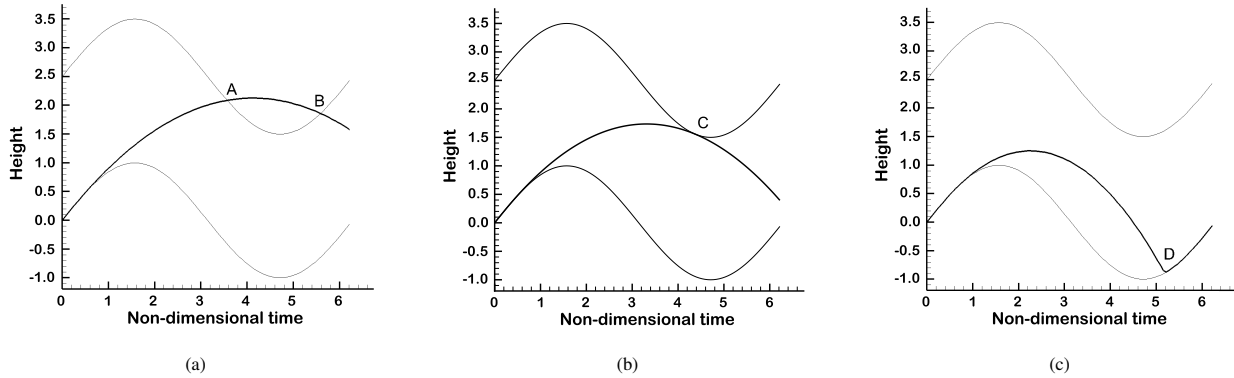

Figure 18: Possible intersection scenarios; (a) Top intersection, (b) Glancing intersection, (c) Bottom intersection

The ballistic-harmonic collision model along with the assumptions and the notation used in this work was introduced in section 2. Depending on the Fr number, the liquid modelled as a lumped mass may intersect the tank's boundaries in different ways. Figure 18 shows different types of ballistic-harmonic intersection. For low Fr the mass does not depart the lower wall, then as Fr increases it skips on the bottom wall (figure 18c), before finally contacting the upper wall (figure 18b) and then entering a sequence of lower/upper wall collisions. If the spacing of the walls is large and Fr high, then it is also possible the mass may skip over multiple periods before landing again on the lower wall, although this is unlikely to be representative for the purposes of this work. The glancing case of figure 18b is critically important, because it represents the watershed before which there is only a single (lower) collision per cycle, and after which there are two collisions per cycle (one upper, one lower) and the number of collisions per period must clearly strongly influence the level of dissipation.
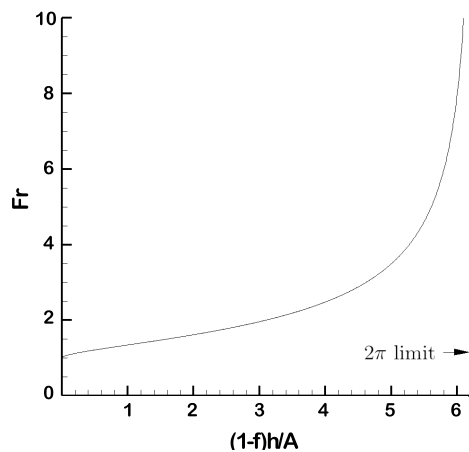

Figure 19: Critical Fr for a glancing impact on the upper wall

30

The value of Fr required to achieve a glancing upper wall collision may be found for any value of $(1-f)h/A$ using the iterative methods in appendix 7, and this is plotted in figure 19. On first inspection it is not clear why a limit exists at 2π, but this is readily explained by considering the case where the ballistic path begins at $t = 0$ and then makes a precisely glancing collision with the upper wall again at $\omega t_h = 2\pi$, which can only be true if Fr is so high that the path of flight is straight (or equivalently that gravity is negligible). This condition corresponds to

$$\sin(\omega t_h) + (1-f)h = \omega A t_h \tag{14}$$

and so knowing that $\sin(\omega t_h) = 0$ gives $(1-f)h/A = 2\pi$. Note that this does *not* mean that at a lower Fr no upper wall collision is possible, only that it could not be tangential at the point of contact. From a practical fluid damping perspective the 2π limit condition is unimportant, because with Fr high the fluid fragments and the model ceases to be representative; the limit would likely be more relevant for a non-fluid system consisting of multiple rigid bodies.

The numerical model presented here is similar to that of Friend and Kinra [30], but has been used to produce full parameter sweeeps of dissipation in the Fr and $(1-f)h/A$ space, as well as to extract the curve giving fill for maximum damping as a function of Fr, which Friend and Kinra did not directly address. The results given here are also not specific to the case of a device mounted on the tip of a beam, but are for the general forced motion case of a container. In addition, the plot of Fr versus $(1-f)h/A$ has been extended to a wider range, and aspects of limit behaviour have been discussed.

6. Time-marching ballistic-harmonic model

Although an iterative solution (see appendix 7) for a limit case is useful, a short numerical model of the output energies associated with the different collision types helps to clarify which intersections are relevant for varying inputs, and permits easy parameter sweeps. The premise is simple; a mass is launched on a ballistic path whenever the wall in which it is in contact with exceeds the acceleration of gravity (lower wall) or is greater than gravity (upper wall). When the subsequent ballistic path terminates, an energy measure defined as

$$K = \frac{\frac{1}{2}m_w v_{rel}^2}{m_w} = \frac{1}{2}v_{rel}^2 \tag{15}$$

may be found where $v_{rel} = v_{water} - v_{wall}$. This measure results in an inelastic model where it is presumed that all kinetic energy available to the impacting dissipative process is lost in each collision, and where the water is immediately forced back to the wall velocity. The value is then normalised as

$$E_c = \frac{K}{\omega^2 A^2} \tag{16}$$

where K is found for one period of forced motion (ie. the dissipation per cycle). It is reasonable to expect that the energy dissipated depends on (i) the number of wall impacts N in a cycle and (ii) the kinetic energy available to be

31

dissipated in each impact. The non-dimensional energy that can potentially be dissipated in a single period of motion can then be written as

$$E_c = \frac{N f_e m_w \omega^2 A^2}{2\omega^2 A^2} \tag{17}$$

where f_e is the fraction of energy dissipated in a collision (here assumed $f_e = 1$), and if this is measured as a power (energy over time, where time is the period $T = 2\pi/\omega$) this leads to the normalised dissipation power, written as

$$P_c = \frac{N f_e m_w \omega^3 A^2}{4\pi m_w \omega^3 A^2} = \frac{N f_e}{4\pi} \tag{18}$$

Note that the existence of a limit does not imply the limit value is the maximum value. It is possible to go further with this line of reasoning; if working in per cycle quantities then the dissipation function is roughly $N f_e/2$. At low Fr only one impact is expected per cycle, rising to two after the upper wall glancing case (the Fr boundary for which is given in figure 18b). This suggests the dissipation limit would be around $2f_e/2 = f_e$, which is quite close to the limit value seen experimentally (see figure 4) given the sweeping simplifications of this argument. The value of f_e is likely to be between 1, for which a mass with speed ωA collides with a stationary wall, and 4, for which a mass with speed ωA collides with a wall moving in the opposite direction with speed $-\omega A$. Broadly speaking, this agrees with the experimental observations. In terms of the ballistic-harmonic model, the dissipation limit corresponds to the upper and lower collision speeds once the parabola is nearly straight, and at that point dissipation is only a function of $(1 - f)h/A$ because dependence on Fr has vanished. In the high Fr limit, the two straight lines prior to each wall collision intersect the sine wave at a fixed angle, which sets the saturation dissipation in this model.
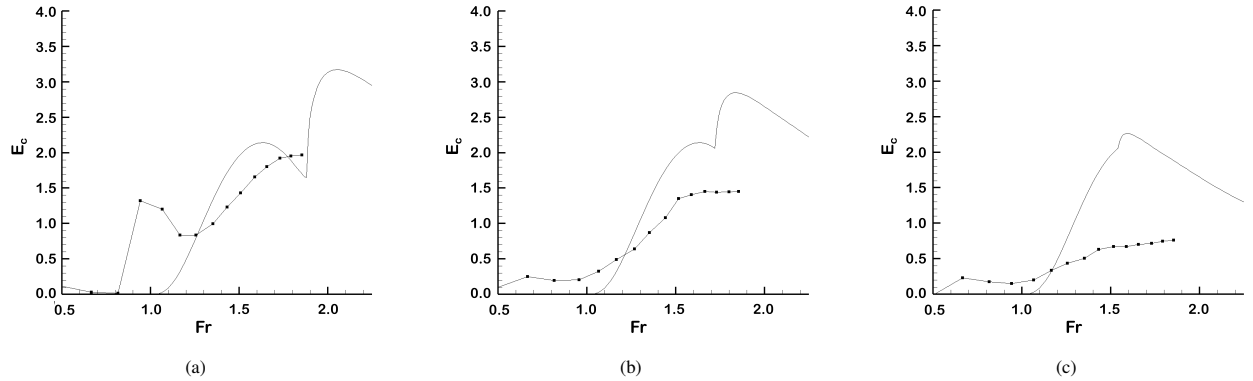

Figure 20: Comparison of dissipation between ballistic-harmonic analytical results (line) and experiment (line-dot); (a) $f = 0.3$, (b) $f = 0.5$, (c) $f = 0.7$

Moving beyond approximate arguments, figure 20 shows comparisons between the time integrated ballistic-harmonic model and experiment. A first important point is that the general trend of increasing dissipation after $Fr = 1$ is captured for the three filling levels, confirming at least a qualitative level of accuracy. The ballistic-harmonic model cannot capture the early peak in dissipation for $f = 0.3$, because this is driven by excitation of free surface sloshing modes rather than ballistic-harmonic collisions. All three fill levels show a cusp in the dissipation, most obviously for

$f = 0.3$. This is due to a different phenomenon, which is that just before the upper wall collision starts happening, the collision speed on the lower wall is diminishing. Once the upper wall collision happens, the lower collision suddenly moves to an earlier point on the sine wave, very quickly increasing the collision velocity and thus the dissipation. This phenomenon is the origin of the cusp, which can be confirmed through the iterative procedure in appendix 7 (or by referring to figure 19) and gives the transition limit values presented in table 3.

f	$(1-f)h/A$	Transition Fr
0.3	2.75	1.86
0.5	2.34	1.72
0.7	1.75	1.54

Table 3: Transition Fr numbers from one to two impacts

The transition point prediction shows that the ballistic-harmonic model correctly mimics the earlier transition to limit dissipation for higher fill values. The physical reason for this is clear; the fuller the tank, the lower the Fr required to achieve an upper wall collision and trigger the critical switch from one to two collisions per cycle. The cusp is not seen in experimental results, because fluid fragmentation progressively prevents it from behaving exactly as a single lumped mass.

There is a mismatch between the analytical and experimental curves presented in figure 20. Ignoring the low excitation amplitudes ($Fr < 1$) that the analytical model cannot predict, the mismatch between the two sets of data increases with filling level. Again, the fluid's behaviour might show why this is the case; while at low filling levels the liquid impacts the tank altogether around one time instance, at high filling levels there is substantial internal mixing inside the liquid, bubble formation and even fluid regions which do not get detached from the bottom of the tank. Moreover, it has been shown previously that when an impact-based model is used for such sloshing modelling, a coefficient of restitution different than 1 is needed to match the energy dissipation rates [8], meaning that only part of the fluid's kinetic energy is transferred during one collision. The model described in this paper uses perfectly inelastic impacts (or an effective coefficient of restitution of 1). These observations based on the fluid's behaviour and modelling suggest that perhaps an equivalent liquid mass may be used to account for different fractions of the liquid participating in a collision.

A final detail to figure 20 is the drop in dissipation after the peak has been reached. This effect is not due to changes in Fr, but is rather driven by replicating the manner in which the experiments were performed. To avoid certain free surface modes, ω was held fixed while A was increased in order to increase Fr. This has the effect of changing not only Fr but also $(1-f)h/A$. Figure 21 shows the landscape of dissipation in terms of Fr and $(1-f)h/A$, revealing that for smaller values of this parameter the dissipation decays if Fr is constant. In the experiments, neither parameter was fixed, so the ballistic-harmonic results follow a particular path that moves to lower values along the $(1-f)h/A$ axis. This itself is equivalent to a fuller, lower height tank at a larger amplitude, which leaves little scope
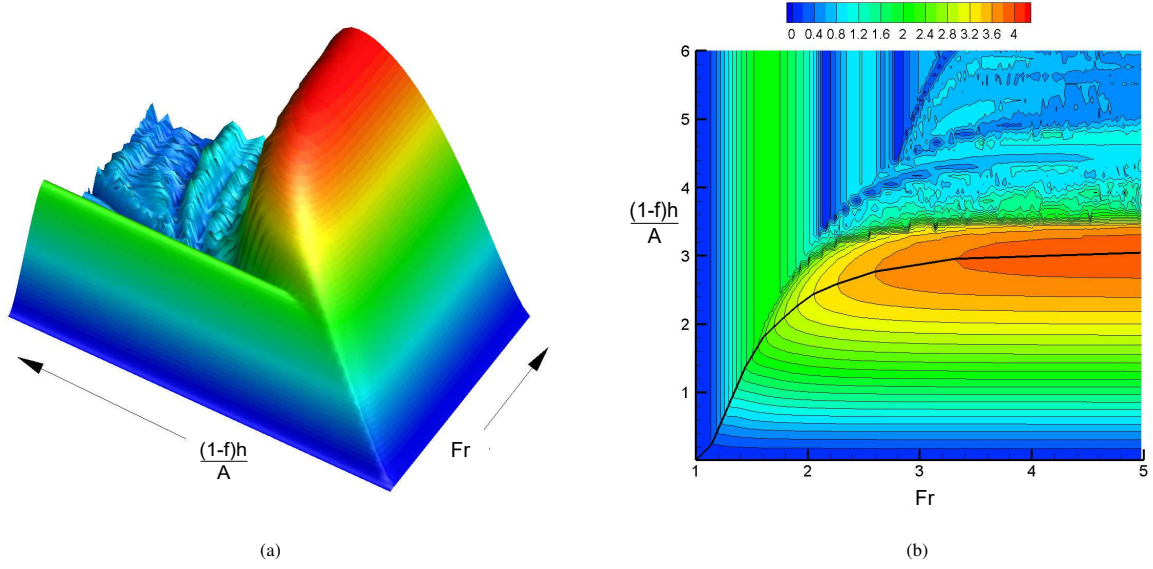
Figure 21: Dissipation function flood plots; (a) Landscape of dissipation function, (b) Contour plot of dissipation, with trajectory of maximal dissipation sketched as bold line

for high relative speed impacts, and causes a progressive decrease in dissipation. If calculations are performed for a variation only in Fr, a clear limit is seen as in figure 21a.

Similar plots have been obtained in Friend and Kinra [30] (figure 16 in their paper). Their results show dissipation increasing and then decreasing in a manner identical to figure 20, for three different filling levels of lead dust. As the filling level of lead is increased, their curves drop, just as those in figure 20 drop as the fluid fill is increased. Furthermore, their numerical calculations also show the same cusp behaviour as in figure 20. Figure 7 in Friend and Kinra's work also shows the same behaviour for the glancing impact case (described in their work as the 'osculating' case) as figure 19 but in their figure it is specific to their studied beam, whereas in this work is it plotted for a general container.

A final question focuses on which filling level maximizes energy dissipation. Figure 21b sketches the trajectory of maximal dissipation with Fr by joining the touching points of the dissipation contours as Fr increases. This clearly reveals that at high Fr, maximal dissipation is for a value of $(1 - f)h/A$ of near 3. The value of 3 is no coincidence; since dissipation is maximised by maximising the collision velocity, in the case of high Fr where the path of flight is straight, it is clear this collision velocity is maximal when $(1 - f)h/A = \pi$, so that the collision occurs at the point of fastest descent for the upper wall. This result implies maximal dissipation for $f \approx 1 - \pi/(h/A)$. Quite often h/A values are 5 to 6, suggesting f of near 0.5. However, at lower values of Fr the fill level for maximal dissipation is Fr dependent, and yields maximal damping at $(1 - f)h/A = 1.5$ for around $Fr = 1.5$, which gives $f = 0.5$ for $h/A = 3$. It is therefore not true that maximal dissipation always occurs at exactly 50% fill, but for common h/A and Fr values this is a surprisingly accurate benchmark.

Attempts were made to derive an analytical expression for the value of $(1 - f)h/A$ that maximises dissipation, but this was only possible when ignoring the secondary lower wall impact due to the non-analytical nature of the curve intersection. It is worth pointing out that the dissipation being maximised here is effectively per unit mass of fluid, such that maximising total dissipation rather than specific dissipation would require including an additional f term in the relative speed. Although useful, this would be case-specific, because h/A would then need to be chosen, and is therefore not pursued here.

The trend in fill level for maximal dissipation follows a straightforward explanation. High dissipation demands (i) a high collision speed and (ii) the existence of an upper wall collision as well as a lower wall collision, so that there are two collisions per cycle, as discussed. Ensuring (ii) for low Fr values demands that the free surface is close to the upper wall, hence the trend to higher fill levels at lower Fr (see bold line in figure 21b). Once Fr is high enough to ensure (ii), then optimal fill level is driven by (i), which requires a sufficient gap to exist between the free surface and the upper wall so that the largest collision speed may be produced.

Finally, it is evidently of fundamental importance that dissipation results for water (as presented here) and lead dust (as presented in [30]) show the same qualitative trends, and can be approximated using the same mechanical model. Although numerical results in each case of course differ, it is conclusive evidence that the dissipative behaviour has at its core the kinematics of ballistic-harmonic motion, rather than the Navier-Stokes equations or their equivalents for a particle system. Exact numerical dissipation values are driven by the fluid or particle behaviour in each case, but it seems the shape of the curves is not.

This concludes the useful information available from this elementary model. Many of the general trends predicted are borne out in experimental results, but the model retains fundamental limitations in terms of being unable to capture free surface modes and in not replicating fragmentation of the fluid. Despite this, the qualitative agreement makes a strong case that much of the dissipation behaviour is driven by ballistic-harmonic kinematics as well as fluid dynamic behaviour, and lends simple insights into what is otherwise a perplexing system.

7. Conclusions

An experimental investigation was performed considering the vertical harmonic motion of a rectangular tank containing a fluid and the resulting sloshing motion and damping, with an emphasis on the amplitude dependent transition between a classical sloshing motion to a turbulent, vertical impacting motion. This experimental campaign provides a comprehensive characterisation of sloshing-induced damping across a large range of excitation amplitudes under controlled conditions. Various image processing techniques were applied to high-speed experimental video footage and the correlation between subtle changes in fluid behaviour and the measured dissipated energy was demonstrated. Qualitative and quantitative explanations were provided for the damping saturation point and general dissipation effects along with measures to distinguish the different sloshing regimes and an understanding of the underlying physical mechanisms. Further studies examined the use of a prescribed vertical harmonic motion of varying amplitudes

tuned to isolate the first symmetric sloshing mode (2,0) where an in-depth hysteresis cycle analysis showed the relation between the sloshing force and the fluid movement, revealing substantial changes in force response and various time asymmetries depending on the Froude number. An asymmetry in sloshing-induced dissipation was observed in two consecutive tank cycles at low excitation amplitudes (Fr < 1.1), which was attributed to liquid-wall shearing asymmetry inside one liquid sloshing cycle.

Comparison with previous experimental results obtained from a different transient system showed very good agreement. Furthermore, in order to shed light on the physics of the violent vertical interaction between the sloshing liquid and the tank, an analytical description of the sloshing motion based on the moment of impact was proposed; the analytical model showed the emergence of the damping saturation limit, as found experimentally, and provided meaningful insights into its nature. The results presented in this work lead to a better understanding of the ways the sloshing motion may be exploited for increased damping in more complex systems such as a commercial aircraft wing, where the excitation mechanism is similar to the one considered here.

Appendix A. Conversion of damping ratio to energy dissipated per cycle

The T-beam transient experiment presented in [8] was shown to behave as a single degree of freedom, viscously damped system described by the equation:

$$z(t) = Ae^{-\zeta \omega t} \cos \omega t \tag{A.1}$$

with ζ being damping ratio measured for the first part of the transient.
The potential and kinetic energies of the system can be obtained:

$$U(t) = \frac{1}{2}kz(t)^2 = \frac{1}{2}kA^2[e^{-\zeta \omega t} \cos \omega t]^2 \tag{A.2}$$

$$T(t) = \frac{1}{2}m\dot{z}(t)^2 = \frac{1}{2}kA^2\left[e^{-\zeta \omega t}\left(\zeta \cos \omega t + \sqrt{1 - \zeta^2} \sin \omega t\right)\right]^2 \tag{A.3}$$

The total energy is $E(t) = T(t) + U(t)$ and can be analysed for each cycle. The total energy can be evaluated at the beginning and end of any transient cycle and, by evaluating the lost energy inside one cycle and normalizing it, we can obtain an expression for the normalized energy dissipated per cycle:

$$E_c = \frac{E((n + 1)T) - E(nT)}{m_w \omega^2 A(nT)^2} \tag{A.4}$$

where n is the cycle number considered. By substituting with the energy terms from equations A.2 and A.3 we obtain:

$$E_c = \frac{1}{2}\frac{k}{m_w \omega^2}(1 + \zeta^2)(e^{-4\pi \zeta} - 1) \tag{A.5}$$

36

where $k \neq m_w \omega^2$ because the normalizing mass is that of the liquid. Equivalently, it can be represented using a mass ratio form:

$$E_c = \frac{1}{2}\frac{M}{m_w}(1 + \zeta^2)(e^{-4\pi\zeta} - 1) \tag{A.6}$$

where M is the structural mass.

Appendix B. Iterative ballistic-harmonic intersections

The intersection of the parabolic flight with the harmonic position of the upper wall is given by

$$-\frac{1}{2}g(t_h - t_s)^2 + \omega A(t_h - t_s)\cos(\omega t_s) + A\sin(\omega t_s) = (1 - f)h + A\sin(\omega t_h) \tag{B.1}$$

$$-\frac{1}{2}\frac{g}{\omega^2 A}\omega^2(t_h - t_s)^2 + \omega(t_h - t_s)\cos(\omega t_s) + \sin(\omega t_s) = \frac{(1 - f)h}{A} + \sin(\omega t_h) \tag{B.2}$$

$$-\frac{1}{2}\frac{1}{Fr^2}\omega^2(t_h - t_s)^2 + \omega(t_h - t_s)\cos(\omega t_s) + \sin(\omega t_s) = \frac{(1 - f)h}{A} + \sin(\omega t_h) \tag{B.3}$$

where f is the fill fraction and $g = 9.81 m/s^2$, t_h is the time when the mass hits a wall, and t_s is the time when it detaches from the lower wall, found from

$$\omega^2 A\sin(\omega t_s) = g \tag{B.4}$$

$$\sin(\omega t_s) = \frac{1}{Fr^2} \tag{B.5}$$

Unfortunately due to the quadratic/harmonic nature of equation B.3 in terms of ωt_h it is not readily solvable for ωt_h. However, a variety of functional iterations readily find the necessary solutions. The first upper wall collision comes from

$$(\omega t_h)_{i+1} = \left(\frac{\frac{(1-f)h}{A} + \sin(\omega t_h) + \frac{1}{2}\frac{1}{Fr^2}\omega^2(t_h - t_s)^2 - \sin(\omega t_s)}{\cos(\omega t_s)} + \omega t_s\right)_i \tag{B.6}$$

The second upper wall intersection, which is not physically relevant but instructive to calculate, comes from

$$(\omega t_h)_{i+1} = \left(\sqrt{-2Fr^2\left(\frac{(1-f)h}{A} + \sin(\omega t_h) - \sin(\omega t_s) - \omega(t_h - t_s)\cos(\omega t_s)\right)} + \omega t_s\right)_i \tag{B.7}$$

The first lower wall impact in the case where the upper wall is not struck first comes from removing the offset $(1-f)h/A$

$$(\omega t_h)_{i+1} = \left(\sqrt{-2Fr^2(\sin(\omega t_h) - \sin(\omega t_s) - \omega(t_h - t_s)\cos(\omega t_s))} + \omega t_s\right)_i \tag{B.8}$$

The case when there is a glancing impact on the upper wall is of interest but also somewhat more difficult to extract, because both ωt_h and Fr are now unknowns. The second equation to close the system is that the velocities must match for a glancing strike, so that

$$\omega A\cos(\omega t_h) = \omega A\cos(\omega t_s) - g(t_h - t_s) \tag{B.9}$$

$$\cos(\omega t_h) = \cos(\omega t_s) - \frac{g}{\omega^2 A}\omega(t_h - t_s) \tag{B.10}$$

from which

$$\cos(\omega t_h) = \cos(\omega t_s) - \frac{1}{Fr^2}\omega(t_h - t_s) \tag{B.11}$$

and this may be used iteratively as

$$Fr_{i+1}^2 = \left(\frac{\omega(t_h - t_s)}{\cos(\omega t_s) - \cos(\omega t_h)}\right)_i \tag{B.12}$$

The process is then to iterate both equation B.3 and equation B.12 in the same loop to give the Fr and ωt_h for the glancing strike case.

The above iterations occasionally require relaxation such that the iterate, be it ωt_h or Fr receives a fraction less than one of its full update.

One further limit case is useful, which is when Fr is very high. In this case gravity is irrelevant and the mass follows a straight path until intersection with the offset sine wave. This gives $\cos(\omega t_s) = 1$, $\sin(\omega t_s) = 0$ and $t_s = 0$ because the mass will detach as soon as the sign of the acceleration swaps, so

$$\omega t_h = \frac{(1-f)h}{A} + \sin(\omega t_h) \tag{B.13}$$

Iterating as

$$(\omega t_h)_{i+1} = \left(\frac{(1-f)h}{A} + \sin(\omega t_h)\right)_i \tag{B.14}$$

References

[1] K.F. Merten & B.H. Stephenson, Some dynamic effects of fuel motion in simplified model tip tanks on suddenly excited bending oscillations, Report, September 1952; (https://digital.library.unt.edu/ark:/67531/metadc56319/: accessed January 20, 2021), University of North Texas Libraries, UNT Digital Library, https://digital.library.unt.edu; crediting UNT Libraries Government Documents Department.

[2] E. Widmayer & J. Reese, Moment of inertia and damping of fluid in tanks undergoing pitching oscillations, NACA Technical Report, 1953.

[3] J.R. Reese, Some Effects of Fluid in Pylon-Mounted Tanks on Flutter, Report, July 19, 1955, (https://digital.library.unt.edu/ark:/67531/metadc61466/: accessed January 20, 2021), University of North Texas Libraries, UNT Digital Library, https://digital.library.unt.edu; crediting UNT Libraries Government Documents Department.

[4] J.L. Sewall, An experimental and theoretical study of the effect of fuel on pitching-translation flutter, NACA Technical Report, 1957.

[5] G. Keulegan, Energy dissipation in standing waves in rectangular basins. Journal of Fluid Mechanics, 6(1), 33-50, 1959, doi:10.1017/S0022112059000489

[6] L. Jiang, M. Perlin & W.W. Schultz, Period tripling and energy dissipation of breaking standing waves, Journal of Fluid Mechanics, vol 369 pp 273-299, 1998, doi:10.1017/S0022112098001785

[7] N. Cavalagli, C. Biscarini, A.L. Facci, Filippo Ubertini & S. Ubertini, Experimental and numerical analysis of energy dissipation in a sloshing absorber, Journal of Fluids and Structures 68 (2017) 466–481, https://doi.org/10.1016/j.jfluidstructs.2016.11.020

[8] L. Constantin, J. De Courcy, B. Titurus, T.C.S. Rendall & J.E.Cooper, Analysis of Damping From Vertical Sloshing in a SDOF System, Mechanical Systems and Signal Processing, 2020, https://doi.org/10.1016/j.ymssp.2020.107452

[9] L. Constantin, J. De Courcy, B. Titurus, T.C.S. Rendall & J.E.Cooper, Sloshing fluid-structure interaction and induced damping effects: modelling and experimental analysis, International Conference on Noise and Vibration Engineering Leuven, Belgium, September 2020

[10] J. De Courcy, L. Constantin, B. Titurus, T.C.S. Rendall & J.E.Cooper, Sloshing induced damping in vertically vibrating systems, 10th EASN Virtual International Conference on Innovation in Aviation & Space to the Satisfaction of the European Citizens, September 2020

[11] R.A. Ibrahim, Liquid Sloshing Dynamics Theory and Application, Cambridge University Press, 2005

[12] T. Ikeda & N. Nakagawa, Non-linear vibrations of a structure caused by water sloshing in a rectangular tank, Journal of Sound and Vibration 201(1), 23–41, 1997

[13] B. Bouscasse, A. Colagrossi, A. Souto-Iglesias & J. L. Cercos-Pita, Mechanical energy dissipation induced by sloshing and wave breaking in a fully coupled angular motion system. I. Theoretical formulation and numerical investigation, Physics of Fluids 26, 033103 (2014); https://doi.org/10.1063/1.4869233

[14] B. Bouscasse, A. Colagrossi, A. Souto-Iglesias & J. L. Cercos-Pita, Mechanical energy dissipation induced by sloshing and wave breaking in a fully coupled angular motion system. II. Experimental investigation, Physics of Fluids 26, 033104 (2014); https://doi.org/10.1063/1.4869234

[15] Y. Tamura, K. Fujii, T. Ohtsuki, T. Wakahara & R. Kohsaka, Effectiveness of tuned liquid dampers under wind excitation, Engineering Structures, Volume 17, Issue 9, 1995, Pages 609-621, https://doi.org/10.1016/0141-0296(95)00031-2

[16] P. Warnitchai & T. Pinkaew, Modelling of liquid sloshing in rectangular tanks with flow-dampening devices, Engineering Structures, Volume 20, Issue 7, July 1998, Pages 593-600, https://doi.org/10.1016/S0141-0296(97)00068-0

[17] Faltinsen, O.M., Firoozkoohi, R. & Timokha, A.N. Analytical modeling of liquid sloshing in a two-dimensional rectangular tank with a slat screen. J Eng Math 70, 93–109 (2011). https://doi.org/10.1007/s10665-010-9397-5

[18] Mi-An Xue, Jinhai Zheng, Pengzhi Lin, Xiaoli Yuan, Experimental study on vertical baffles of different configurations in suppressing sloshing pressure, Ocean Engineering, Volume 136, 2017, Pages 178-189, ISSN 0029-8018, https://doi.org/10.1016/j.oceaneng.2017.03.031.

[19] E. Demirel & M.M. Aral, Liquid Sloshing Damping in an Accelerated Tank Using a Novel Slot-Baffle Design, Water 2018, 10, 1565. https://doi.org/10.3390/w10111565

[20] A. Colagrossi, F. Palladino, M. Greco, C. Lugni & O. Faltinsen, Experimental and numerical investigation of 2D sloshing : scenarios near the critical filling depth, Proc. 19th International Workshop on Water Waves and Floating Body, Cortona, Italy, 2004

[21] Olav F. Rognebakke & Odd M. Faltinsen, Sloshing induced impact with air cavity in rectangular tank with a high filling ratio, Proc. 20th International Workshop on Water Waves and Floating Bodies, Vol. 1, 2005

[22] Olav F. Rognebakke & Odd M. Faltinsen, Damping of sloshing due to roof impact, Proc. 15th International Workshop on Water Waves and Floating Bodies, Ceasarea, Israel, 2000

[23] Molin, B, Remy, F, Ledoux, A, & Ruiz, N., Effect of Roof Impacts on Coupling Between Wave Response and Sloshing in Tanks of LNG-Carriers, Proceedings of the ASME 2008 27th International Conference on Offshore Mechanics and Arctic Engineering. Volume 6, Estoril, Portugal. June 15–20, 2008. pp. 15-24. ASME. https://doi.org/10.1115/OMAE2008-57039

[24] J. Martinez-Carrascal, L.M. González-Gutiérrez, Experimental study of the liquid damping effects on a SDOF vertical sloshing tank, Journal of Fluids and Structures, Volume 100, 2021, 103172, ISSN 0889-9746, https://doi.org/10.1016/j.jfluidstructs.2020.103172.

[25] J. Calderon-Sanchez, J. Martinez-Carrascal, L. M. Gonzalez-Gutierrez & A. Colagrossi, A global analysis of a coupled violent vertical sloshing problem using an SPH methodology, in process of publication

[26] B. Titurus, J.E. Cooper, F. Saltari, F. Mastroddi & F. Gambioli, Analysis of a Sloshing Beam Experiment, International Forum on Aeroelasticity and Structural Dynamics (IFASD 2019), Savannah, Georgia, USA, June 2019

[27] F. Gambioli, R.A. Usach, J. Kirby & T. Wilson, Experimental Evaluation of Fuel Sloshing Effects on Wing Dynamics, International Forum on Aeroelasticity and Structural Dynamics (IFASD 2019), Savannah, Georgia, USA, June 2019

[28] J. De Courcy, L. Constantin, B. Titurus, T.C.S. Rendall & J.E.Cooper, Gust Loads Alleviation Using Sloshing Fuel, AIAA Scitech 2021 Forum, VIRTUAL EVENT, January 2021, https://doi.org/10.2514/6.2021-1152

[29] F. Mastroddi, F. Saltari, A. Traini, A. Barile & F. Gambioli, Sloshing ROMs for Fluid-Structure Interactions in Aerospace Applications, AIAA 2020-1451, Session: Numerical Techniques for Fluid-Structure Interaction Published Online: 5 Jan 2020, https://doi.org/10.2514/6.2020-1451

[30] R.D. Friend & V.K. Kinra, Particle Impact Damping, Journal of Sound and Vibration (2000) 233(1), 93 - 118 doi:10.1006/jsvi.1999.2795

[31] R. A. Ibrahim, Recent Advances in Physics of Fluid Parametric Sloshing and Related Problems, ASME. J. Fluids Eng. September 2015; 137(9): 090801. https://doi.org/10.1115/1.4029544

[32] W. Froude, The Papers of William Froude, 1810-1879: With a Memoir by Sir Westcott Abell and an Evaluation of William Froude's Work

by R.W.L. Gawn, Published by Institution of Naval Architects (1955)

[33] R. Alexander, The Gaits of Bipedal and Quadrupedal Animals, The International Journal of Robotics Research. 3 (2): 49–59, 1884. doi:10.1177/027836498400300205.

[34] O. M. Faltinsen & A. N. Timokha, Sloshing, Cambridge University Press, 2009

[35] J. Calderon-Sanchez, J. Martinez-Carrascal, L.M. Gonzalez-Gutierrez & A. Colagrossi, A global analysis of a coupled violent vertical sloshing problem using an SPH methodology, in process of publication

[36] O. M. Faltinsen, O. F. Rognebakke, & A. N. Timokha, Transient and steady-state amplitudes of resonant three-dimensional sloshing in a square base tank with a finite fluid depth, Physics of Fluids 18, 012103 (2006); https://doi.org/10.1063/1.2160522

[37] A. Masullo, R. Theunissen, Automated mask generation for PIV image analysis based on pixel intensity statistics. Exp Fluids 58, 70 (2017). https://doi.org/10.1007/s00348-017-2357-3

[38] H. Bredmose, M. Brocchini, D. Peregrine, & L. Thais, Experimental investigation and numerical modelling of steep forced water waves. Journal of Fluid Mechanics, (2003), 490, 217-249. doi:10.1017/S0022112003005238

[39] F. T. Dodge, D. D. Kana, H. N. Abramson, Liquid surface oscillations in longitudinally excited rigid cylindrical containers, AIAA JOURNAL Vol. 3 No. 4, April 1965, https://doi.org/10.2514/3.2948

[40] J.W. Miles, Surface-wave damping in closed basins, Published by Royal Society (1967) https://doi.org/10.1098/rspa.1967.0081

Acknowledgement